Aberrant Connectivity Across the Lifespan in a Mouse Model of Alzheimer's Disease and Rescue by mGluR5 Modulator Treatment

Francesca Mandino[1], Xilin Shen[1], Gabriel Desrosiers-Gregoire[2,3], David O'Connor[4], Bandhan Mukherjee[5], Ashley Owens[5], An Qu[1], John Onofrey[1,6], Xenophon Papademetris[1,7], Mallar Chakravarty[2,3,8,9], Stephen M Strittmatter[5,10,11,12*], Evelyn MR Lake[1*]

[*] Co-senior authorship

Correspondence: stephen.strittmatter@yale.edu or evelyn.lake@yale.edu

[1] Department of Radiology and Biomedical Imaging, Yale School of Medicine, New Haven, CT, 06520, USA.
[2] Computational Brain Anatomy Laboratory, Cerebral Imaging Center, Douglas Mental Health University Institute, Montreal, QC, H4H 1R3, Canada.
[3] Integrated Program in Neuroscience, McGill University, Montreal, QC, H3A 0G4, Canada.
[4] Department of Biomedical Engineering, Yale University, New Haven, CT, 06511, USA.
[5] Cellular Neuroscience, Neurodegeneration and Repair Program, Departments of Neurology and Neuroscience, Yale School of Medicine, New Haven, CT, 06520, USA.
[6] Department of Urology, Yale School of Medicine, New Haven, CT, 06520, USA.
[7] Department of Biomedical Engineering, Yale University, New Haven, CT, 06520, USA.
[8] Department of Psychiatry, McGill University, Montreal, QC, H3A 0G4, Canada.
[9] Department of Biological and Biomedical Engineering, McGill University, Montreal, QC, H3A 0G4, Canada.
[10] Department of Neurology, Yale University School of Medicine, New Haven, CT 06510, USA.
[11] Kavli Institute of Neuroscience, Yale University School of Medicine, New Haven, CT 06510, USA.
[12] Department of Neuroscience, Yale University School of Medicine, New Haven, CT 06510, USA.

Keywords. Mouse, functional magnetic resonance imaging, blood oxygen level dependent signal, multimodal imaging, functional connectivity, brain networks, Alzheimer's disease, treatment.

Abstract

Amyloid accumulation in Alzheimer's disease (AD) is associated with synaptic damage and altered connectivity in brain networks. While measures of amyloid accumulation and biochemical changes in mouse models have utility for translational studies of certain therapeutics, preclinical analysis of altered brain connectivity using clinically relevant fMRI measures has not been well developed for agents intended to improve neural networks. Here, we conduct a longitudinal study in a double knock-in mouse model for AD (*App*$^{NL\text{-}G\text{-}F}$/*hMapt*), monitoring brain connectivity by means of resting-state fMRI. While the 4-month-old AD mice are indistinguishable from wild-type controls (WT), decreased connectivity in the default-mode network is significant for the AD mice relative to WT mice by 6 months of age and is pronounced by 9 months of age. In a second cohort of 20-month-old mice with persistent functional connectivity deficits for AD relative to WT, we assess the impact of two-months of oral treatment with a silent allosteric modulator of mGluR5 (BMS-984923) known to rescue synaptic density. Functional connectivity deficits in the aged AD mice are reversed by the mGluR5-directed treatment. The longitudinal application of fMRI has enabled us to define the preclinical time trajectory of AD-related changes in functional connectivity, and to demonstrate a translatable metric for monitoring disease emergence, progression, and response to synapse-rescuing treatment.

Introduction

It can take decades for the hallmarks of Alzheimer's disease (AD) to fully manifest. Optimistically, this is evidence of a long therapeutic window during which treatment could interrupt or reverse disease processes if we had robust ways of identifying patients, staging disease, and access to effective therapeutics. As a noninvasive imaging modality that measures brain-wide activity patterns, functional magnetic resonance imaging (fMRI) is a good candidate for helping to address these needs. Indeed, BOLD (blood-oxygen-level dependent) fMRI, when acquired at rest (without stimuli or tasks), yields measures of functional connectivity (FC, or inter-regional BOLD signal synchrony), which show progressive AD-related changes with brain network specificity [1-4]. Encouragingly, disrupted FC emerges years prior to overt symptoms (in patients with mild cognitive impairment and asymptomatic people with genetic risk factors for AD[5,6]), progresses in concert with declines in executive function and cognition, and follows a similar trajectory of spatial patterning as subsequent brain atrophy, Aβ-pathology and neurofibrillary tangle deposition [7,8], as well as synapse loss [9-12]. Thus, BOLD-fMRI FC may be sensitive to many of the varied stages of AD emergence and progression. However, despite tremendous effort, and investment, human fMRI research has yet to produce actionable bioimaging markers of AD[2]. In part, this is due to the long time-scale and complexity of AD pathology, the difficulty of relating non-invasive imaging markers to underlying mechanisms, and the substantial heterogeneity in the population.

To accelerate progress towards improving our understanding of the BOLD-fMRI correlates of AD and how we might use this modality for patient management, we can apply BOLD-fMRI in animal models of the disease[13-15]. Studies in animals provide a well-controlled environment for measuring disease phenotypes, for testing therapeutics on a tractable timescale, and for increased freedom to use invasive techniques. The short lifespan, low-cost, and genetic malleability of mice, together with recent improvements in rodent BOLD-fMRI data quality and processing techniques [16-20] (including inter-species translation [21,22]), mean the field is well-positioned to make new inroads into AD research. Advances in how we model AD in mice, where it has been hard to faithfully recapitulate human disease [23], lends further cause for enthusiasm. Here, we use the double-knock-in (DKI) *App*$^{NL\text{-}G\text{-}F}$*/hMapt* (amyloid-precursor-protein/human microtubule-associated protein tau) mouse model[24,25], which critically avoids

overexpression artifacts. We collect longitudinal resting-state BOLD-fMRI data spanning a wide-range of AD-relevant timepoints from 4 to 22 months of age (M), or the rough equivalent of 20-70 years of age in humans[26], to measure changes in brain functional organization using FC. In late-stage disease (20-22M), we treat a subgroup of mice with a metabotropic glutamate receptor 5 (mGluR5) silent allosteric modulator (BMS-984923[27]). This compound is known to modify AD course by rescuing synapses and improving memory[28], and has recently entered clinical trials (ClinicalTrials.gov; NCT05804383). However, the treatment-elicited effects on BOLD-fMRI FC are currently unknown. We sought to address this gap in knowledge given the potential usefulness of BOLD-fMRI for monitoring treatment response.

We find that FC in AD mice follows a distinct age-trajectory relative to wild-type (WT) littermates. Age-related changes in WT mice emerge earlier-in-life and are characterized by increases in FC with age. In AD mice, changes emerge later and show more widespread decreases with time. The brain networks we identify using data-driven approaches show significant enrichment for established circuits including the default mode and lateral cortical networks (DMN and LCN, respectively [29,30]). Further, oral treatment with BMS-984923 rescues FC deficits in AD mice. In sum, this work identifies age- and AD-related phenotypes in resting-state BOLD-fMRI data across the mouse lifespan in a relevant model of disease[24,25]. We also find timely evidence that resting-state BOLD-fMRI FC may prove useful for measuring the effects of a novel synapse-rescuing AD treatment.

Results

Male and female mice (N=74) from three longitudinal BOLD-fMRI experiments are included (**Table 1**). Prior to imaging, all animals undergo a minimally invasive surgical procedure[31-33], where a head-plate is affixed to the skull a month prior to any imaging (timeline, **Fig. 1**). The implants reduce susceptibility artifacts in the cortex and head-motion. Mice are imaged longitudinally at 4, 6 and 9M (experiment 1), at 6 and/or 9M (experiment 2), and at 20 and 22M (experiment 3). The head-plates are well tolerated and the signal-to-noise ratio (SNR) in the cortex shows no change over time (data not shown, non-significant differences in SNR across sessions). At all imaging timepoints, MRI data are collected from a double knock-in (DKI) mouse model of AD (*App*$^{NL\text{-}G\text{-}F}$*/hMapt*)[24,25] and WT littermate controls. After the 20M imaging timepoint, a subgroup of AD mice are randomly assigned to oral treatment with BMS-984923[27]

($AD_{treated}$) or regular chow ($AD_{vehicle}$). Thirty-minutes of resting-state BOLD-fMRI data, together with structural images for data registration, are collected at each timepoint under low-dose isoflurane (0.5-0.75%). Data are processed and registered to a common space[31,33,34]. A small fraction of the fMRI data (9%) are excluded based on quality control standards[16,34-36]. Z-scored functional connectomes (brain-wide FC measurements) are computed using 172-regions from the Allen Atlas CCfv3[37,38] (key, **Fig. S1**) and Pearson's correlation. Average connectomes for each group at each timepoint are shown in **Fig. 1**. Stereotypical patterns including high FC between bilateral brain regions are observed. Differences between connectomes are displayed with and without thresholding for significance ($p<0.05$) at the edge-level and correcting for multiple comparisons (**Methods**). Permutation testing (by randomly shuffling datasets) is applied (×1,000 iterations). In all results, the test statistic of the null distribution is the number of edges (region-to-region measures of FC) remaining after correcting for multiple comparisons. Identified brain circuits that show significant effects are summarized as connectomes, vertical histograms, circle plots, and node-degree maps.

Age-related changes in functional brain organization diverge between WT and AD mice.

AD progression occurs atop a background of age-related changes in behavior and brain function[39,40]. We examine age-related changes by quantifying differences between connectomes across timepoints: 4 vs. 6M (early), 4 vs. 9M (mid), 4 vs. 20M (late), and 4 vs. 22M (very late), within WT and AD groups (**Fig. 2**). Few early-life age-related changes in FC are identified in either group (**Fig. 2**, permutation test $p<0.05$). Beginning at mid-life, WT mice show a widespread increase in FC (**Fig. 2a,** permutation test $p<0.001$), that is not observed in AD mice (although, a trend in this direction is noticeable in unthresholded and uncorrected data, **Fig. 2b**, permutation test $p<0.05$). This increase, in the WT group, persists until the study endpoint. At 20 and 22M, some decreases in FC are also observed in ventral areas alongside more widespread increases (permutation test $p<0.001$). AD mice show a more modest FC increase with age, and this emerges later, in conjunction with a pronounced decrease in FC within subcortical regions (**Fig. 2b**). Overall, WT and AD groups follow distinct patterns of age-related changes in brain functional organization that unfold along different time-scales. As a control, to account for any differences between

WT and AD mice at 4M, we repeat our analyses using all mice (WT and AD) at 4M as a reference (**Fig. S2**). No differences in outcome patterns are observed.

Regions in WT mice that show pronounced age-related increases in FC beginning at 9M include somatosensory and motor regions (SS/MO), visual cortices (VIS), midbrain (MB), hypothalamus (HY) and the retrosplenial areas (RSP). AD mice show more modest increases in the same areas but starting at 20M. Moreover, AD mice show a more pronounced decrease in FC in the ventral parts of the brain encompassing the hippocampal formation (HF), entorhinal cortex (ENT), ectorhinal and perirhinal regions (ECT, PERI), ventral striatal areas including the caudoputamen (CP), and piriform and insular regions (PIR, INS).

Aging trajectories in WT and AD mice effect overlapping and distinct networks.

In addition to examining which regions are most affected by age, we can quantify over or under enrichment for edges within established or canonical networks. Here, and in following subsections, we use the triple-network model[30,41]: default mode, lateral cortical, and salience networks (DMN, LCN, and SN) as well as the edges that connect them (e.g., DMN to LCN) to characterize the data-driven brain circuits we identify. For a breakdown of the regions within these networks, see **Fig. S1b**. Above (**Fig. 2**), we establish that WT and AD mice show distinct patterns of age-related changes in FC. Here, we define a data-derived 'WT-aging' (**Fig. 3a**) and an 'AD-aging' (**Fig. 3b**) network. We consider both the sum (*all* edges surviving correction, **Fig. 3a,b** left) and the intersect (*common* edges surviving correction, **Fig. 3a,b** middle) at the two indicated timepoints as a comprehensive (sum) and stringent (intersect) definition of our networks. Importantly, we collapse across the two timepoints that show the most pronounced effects: mid & late for WT and late & very late for AD (as indicated in **Fig. 2**). Note that the edges identified in both groups at the chosen stages are highly overlapping (**Fig. 3,** observed jaccard similarity significantly different from a null distribution, $p<0.001$, for both groups).

We compute enrichment (or depletion, under enrichment) for edges within the triple-network model and our aging networks (**Fig. 3a,b** right) using Fisher's exact test as well as permutation testing (×1,000 iterations). Results are corrected for multiple comparisons. We find that the WT-aging positive (+ve) network (older > younger) is enriched for edges in the DMN and LCN as well as edges that connect all

three networks. The WT-aging negative (-ve) network (older < younger) shows under-enrichment (depletion) for DMN to LCN. Further, the AD-aging (+ve) network (older > younger) shows enrichment in the DMN, DMN to LCN and DMN to SN, and under-enrichment in the SN. While the AD-aging (-ve) network (older < younger) shows under-enrichment in the LCN, DMN to LCN and a trend towards under-enrichment in the DMN. In sum, WT and AD mice show some common trends for which networks in the triple-network model are implicated in age-related changes in connectivity strength, but also some clear differences.

Depressed connectivity strength in AD relative to WT mice emerges at 9M.

After establishing aging trajectories for both genotypes (WT and AD), we compute differences between WT and AD connectomes at each timepoint (**Fig. 4**). Edges where FC in AD is greater than WT (AD > WT) are plotted as positive t-values (red). Edges where FC in AD < WT are plotted as negative t-values (blue). Permutation testing is applied (as above). Some very sparse but significant differences between WT and AD mice are observed at early timepoints (4 and 6M, $p<0.05$) with strong effects emerging by 9M (permutation test, $p<0.001$). Overwhelmingly, AD mice show lower FC. Notably, affected areas are bilaterally symmetric and appear throughout the brain but are concentrated in the cortex. Identified regions include the SS, MO, VIS, and RSP areas, as well as regions encompassing the HF, temporal association areas (TeA), nucleus accumbens (ACB), auditory (AUD) and MB areas.

The networks most strongly effected in AD relative to WT are the DMN and LCN.

As above, we investigate the network composition[30,41] of the brain circuits most affected in AD relative to WT mice. The most pronounced differences are observed at 9 and 20M (permutation test, $p<0.001$, **Fig. 4a**) and the edges identified at these timepoints are highly overlapping (observed jaccard similarity vs. null distribution, $p<0.001$). As above, we consider the sum (comprehensive) and intersect (stringent) in our definition of a data-derived 'AD-like network' (**Fig. 4b** left and middle). We find that, at both thresholds, the AD-like (-ve) network (AD < WT) is enriched for edges in the DMN and LCN as well as edges that connect the DMN to the LCN, and LCN to SN (Fisher's exact test; **Fig. 4b** right). This network is also under-enriched for edges that are between the DMN and SN. A trend is noted for under enrichment for edges in the SN. There are no significant AD-like (+ve) network (AD > WT) findings.

Comparison of mouse aging and AD networks with human literature meta-analysis (Neurosynth)

In an exploratory analysis, we use Neurosynth (http://neurosynth.org) to compare our mouse-model data-derived aging and AD-like networks to human neuroimaging studies using the queries 'Age' and 'Alzheimer' (**Fig. S3**). Neurosynth accepts one-word queries and provides 'activation maps' proportional to 'hits' in the literature without directionality (increases/decreases) [42]. As such, our aim is to visualize Age/Alzheimer maps across species for a purely qualitative comparison. **Fig. S3** shows the association test maps (z-scored, corrected for false discovery rate, FDR = 0.01; also see [42]) from human fMRI data next to the node degree maps we obtain from mouse fMRI data. Encouragingly, in each comparison, homologous regions emerge. Specifically, somatomotor, SS, and dorsolateral-prefrontal areas are implicated in (healthy *and* WT) aging across species (**Fig. S3**, top), as are VIS, insula and RSP cortices (i.e., including RSP and precuneus in humans[21]). In AD, subcortical areas, including the HF and TH, appear in both species (**Fig. S3**, bottom).

Treatment with BMS-984923 rescues FC deficits in AD mice at 22M.

After imaging at 20M, half of the mice in the AD group are randomly assigned to treatment with BMS-984923 ($AD_{treated}$). The drug is incorporated into mouse chow to achieve sustained therapeutically effective levels, as documented in our previous study[27]. We characterize treatment effects using three comparisons: (1) 22M WT vs. 22M $AD_{treated}$ (**Fig. 5a**), (2) 22M $AD_{treated}$ vs. 20M $AD_{vehicle}$ (**Fig. 5b**, left), and (3) 22M $AD_{vehicle}$ vs. 22M $AD_{treated}$ (**Fig. 5b**, right). Across all comparisons we observe evidence of treatment effects. In comparison 1, there is a lack of FC differences between 22M WT and 22M $AD_{treated}$ (**Fig. 5a** right, $p>0.5$ for the permutation test), even though there is a persistent difference between 22M WT and 22M $AD_{vehicle}$ (**Fig. 5a** left, reproduced from **Fig. 4**, $p<0.001$ for the permutation test). Comparisons 2 and 3 highlight edges whose strengths change with treatment. We select the brain circuits identified in comparisons 2 and 3 to generate, as before, a comprehensive and a stringent data-derived 'treatment network' (**Fig. 5c**, left and middle). Regions within this network include the VIS, AUD, MB, HY, HF, TH and CP areas. The (+ve) network (treated > vehicle) is under-enriched for edges in the LCN, and edges between the LCN and DMN (**Fig. 5c** right). There are no significant (-ve) network (treated < vehicle) findings. Of note, the difference in FC at 22M between WT and $AD_{vehicle}$ show a smaller effect size relative

to the 20M timepoint. We find that this is likely due to a smaller sample size at the later timepoint by randomly selecting scans at 20M to match the number available at 22M and finding a similarly weakened effect size (data not shown).

Regions that show the highest degree of association with treatment include the VIS, MB, AUD, HY (**Fig. S5**). Notably, these regions also show high-degree representation in the AD-aging and AD-like networks (AD-aging and AD-like in **Fig. S5**) suggesting treatment specific targeting of regions involved in AD (as opposed to indirect or off-target effects of drug treatment).

Mapping the shared functional landscape of data-derived networks

Seven data-derived networks are identified: AD-aging (-ve/+ve), WT-aging (-ve/+ve), AD-like (-ve/+ve) and treatment (+ve). We quantify the amount of cross-network (under) enrichment (as above), i.e., whether there is a significant number of shared edges, (or lack of shared edges), using Fisher's exact test (and permutation testing, ×1,000 iteration), between all pairs of data-derived networks (**Fig. 6**). By definition, there is under-enrichment between AD-aging (+ve) vs. (-ve), and WT-aging (+ve) vs. (-ve) (**Fig. 6a**, **b**). We also find under-enrichment between AD-aging (+ve) vs. WT-aging (-ve), AD-aging (-ve) vs. WT-aging (+ve), and WT-aging (-ve) vs. AD-like (-ve). In addition, two patterns of enrichment emerge: the first between (+ve) aging (AD and WT) and AD-like (-ve), (**Fig. 6e**, left) and the second between treatment (+ve) and AD-aging (-ve), WT aging (+ve), and AD-like (-ve) (**Fig. 6e**, right). The second pattern is weaker, without as many edges, and shows no representation in the triple-network model (i.e., shared edges do not belong to DMN, LCN, SN or their inter-network pairings). Conversely, the first pattern shows a higher proportion of shared edges across network pairs (**Fig. 6a**, **e**, left). Edges shared between AD-aging (+ve) and AD-like (-ve) include 30% of the smaller, AD-like (-ve), network (proportion of shared edges, **Fig. 6a**, is computed as the fraction of the smaller network). Further, this 30% is fully contained within the other two inter-network pairings (**Fig. 6e**, left). The remaining pairings: WT-aging (+ve) vs. AD-aging (+ve) as well as WT-aging (+ve) vs. AD-like (-ve), show an even higher proportion of shared edges (67 and 85%, respectively, **Fig. 6a**), but a more modest inter-network pairing overlap (35%, **Fig. 6e**, left). Edges within the three pairings in the second pattern show a high representation of DMN and LCN, as well as edges that link DMN to LCN, and LCN to SN. Two of the three, AD-aging (+ve) vs. WT-aging

(+ve) and AD-aging (+ve) vs. AD-like (-ve), show under-enrichment for the SN (**Fig. 6c**). Brain regions with high-degree that appear within these inter-network pairings (**Fig. 6d**, **f**) include primary SS, MO, VIS and RSP areas.

Median FC within data-derived networks across the mouse lifespan

The product of each data-derived network and each mouse's connectome is computed at each timepoint. The median FC of nonzero elements are plotted for WT and AD mice (**Fig. 7**, **S6**). The key metric of disease is the AD-like (-ve) network (**Fig 7a**). Median FC in this network is decreased in AD relative to WT mice at 9M and 20M ($p<0.01$), but not at earlier timepoints. At 22 M, the $AD_{vehicle}$ mice show decreased median FC in the AD-like (-ve) network relative to WT and relative to $AD_{treated}$ mice, but AD-treated are indistinguishable from WT. The treatment (+ve) network by definition shows increased median FC in $AD_{treated}$ mice relative to $AD_{vehicle}$ at 22M (**Fig 7b**). There is a significant treatment effect on the AD pathology at the $p<0.001$ level for the two conditions (pathology and treatment; ANOVA, [$F(2,20)=10.48$, $p=0.0008$]). Importantly, this drug-responsive network exhibits statistically significant decreases for AD mice relative to WT mice preceding treatment at 9M and 20M. The WT-aging (+ve) network associated with healthy brain maturation highlights an increase in median FC in WT relative to AD mice at 9M and 20M (**Fig. S6**). Overall, connectivity in these data-driven networks across groups is well-aligned with the specific comparisons above.

Discussion

Non-invasive imaging technologies, including fMRI, applied in animal models of human disease allow aspects of pathology to be characterized in a controlled environment on a tractable timescale and for the assessment of clinically accessible bioimaging markers of disease emergence, progression, and response to treatment. Here, we investigate the BOLD-fMRI correlates of AD, throughout the mouse lifespan, in an optimized model of disease [27,43]. In addition, we investigate the neuroimaging correlates of a novel synapse rescuing treatment (BMS-984923) administered late in life, once AD-like pathology is well established. We uncover networks which characterize aging (with and without disease), disease-associated changes in FC strength, as well as treatment-response. Analyses are conducted using data-driven approaches (i.e., no *a priori* assumptions are made about the roles established brain circuits, e.g.,

DMN, or regions play in these processes). We quantify the presence (or absence) of classic large-scale networks following the discovery phase and examine correspondences across species.

We explore changes in FC strength with age in WT and AD mice at three life-stages: young-adulthood (6M or 20-30 years-of-age in humans), middle-age (9M or 38-47 years), and older-adulthood (20-22M or 56-69 years)[26]. We find FC strength in WT mice follows an inverted-U-shaped profile (**Fig. 2a, S6a**). This pattern is roughly in-line with a small pool of existing work using fMRI in mice [44,45] (**Table 2**). Across studies, relative to baseline (2-4M), there is good agreement that circuit-specific increases in FC strength emerge and peak within 5-9M [44,45]. Between 10-18M (which we do not examine), fMRI [44,45] shows a return to baseline, and optical imaging methods [46] show a dip below baseline (at 17-18M). At 20M, we observe a persistent increase in FC strength, followed by a reduction at 22M. Differences in these collective observations in later-life could be due to a mismatch between timepoints, modalities (optical vs. fMRI), anesthesia (Egimendia et al. and Vasilkovska et al. use medetomidine and isoflurane whereas optical data in the Albertson et al. study is acquired from awake animals), or the specific brain circuits being examined. It is also possible that the inverted-U-shaped profile is incomplete, and the brain follows an even more complex double-humped shaped profile. Despite the small number of existing studies, increased FC strength in mid-life seems to be a relatively reproducible observation. Encouragingly, this inverted-U-shaped profile in fMRI FC strength is also reported in cognitively healthy human subjects. As in mice, middle-aged people show greater FC strength, relative to the young and elderly [47,48].

Further, in mice, we find good agreement across studies in terms of which brain regions show age-related changes in FC strength (**Table 3**). Universally, the DMN – which includes RSP and VIS areas among others – shows age-related changes [47]. MO, ACA, as well as auditory and SS areas also show good-moderate cross-study agreement (given the methodological differences between studies). Notably, these implicated areas include regions that are not typically associated with cognition (e.g., SS and MO areas). We also note strong alignment across species. In humans, the DMN [47,48], as well as ‘cognitive’ and ‘motor’ circuits [49-51] all show age-related changes in FC strength (that generally follow the inverted-U-shaped profile). In the present study, we also observe the LCN (includes SS, TeA, and MO areas), MB, HY, and TH to be involved in WT- aging. Given inter-study difference in how networks are defined, and analyses

conducted (data-driven, vs. *a priori* network or ROI driven), it is unclear whether these findings are unique. Finally, our Neurosynth findings in the human brain associated with age (**Fig. S3**) show considerable overlap (including the TH and TeA) with the regions and networks identified in mice (**Table 3**).

This emerging cross-study (and species) convergence is promising. Yet, there are several competing theories on the neurobiological drivers of healthy aging which have proven difficult to reconcile (see reviews, [52,53]) especially when using fMRI in isolation. Although it is the beyond the scope of the present work to interrogate the mechanisms which give rise to these fMRI-observable age-related changes, we are well positioned to interrogate their origins as part of our future work using multimodal approaches[33,54,55].

Decreases in FC strength (AD vs. control) is an established hallmark of neuropathology in mouse models [13,44,56,57]. Likewise, fMRI measures from humans show a tight association between cognitive decline and lower FC strength [58,59]. Yet, these AD-related changes occur against a non-trivial background of aging that can be overlooked when a single timepoint is considered. Is lower FC strength (in AD vs. control) a result of a decrease in the AD group? Or (as our data suggest, **Fig. 2**, **6**, **7**, **S6**), a failure to increase with maturation? This is likely an important distinction that will require further investigation.

In addition to examining healthy aging, we examine age-related changes in FC strength in AD mice alongside differences between WT and AD groups at each timepoint. Changes in FC strength with age in AD mice (**Fig. 2**) emerge later in life (relative to WT aging) and show more widespread decreases (**Fig. 3**). Yet, there are also preserved common elements between WT and AD aging which are reflected by the high proportion of common circuitry (**Fig. 6**). From our inter-group (AD vs. WT) comparison (at each timepoint), we observe a clear decrease in FC strength by 9M in AD. The directionality of these FC changes (decrease in AD-like models compared to WT) is in-line with previous fMRI work in other mouse models of AD [13-15,56]. Notably, the FC deficits reported here appear later in life (9M) compared to literature (as early as ~3M[13]), which may be a result of the milder nature of the pathology in this mouse model. Critically, the DKI *App*$^{NL\text{-}G\text{-}F}$*/hMapt* model [24,25] investigated here has not previously been examined using fMRI. This is important, as this new model represents a step-forward in our ability to emulate AD-like pathology via its milder genetic profile [60].

The circuits and regions we find to be involved in aging (**Fig. 2**, **3**), WT vs. AD (**Fig. 4**), and their common elements (**Fig. 6**) are summarized in **Table 4**. Only two regions (ACB and HY) show age-related changes uniquely in WT mice, whereas more widespread age-related changes are unique to AD mice (INS, ECT, PERI, CP, and PIR). Regions that do not show age-related changes, but are identified when comparing WT vs. AD include TeA, PPA, ENT, and HF. Most circuits and regions, however, are shared across at least 2/3 comparisons (as expected based on our analyses, **Fig. 6**). Roughly, in order of frequency across comparisons (columns in **Table 4**), we observe involvement of the DMN-to-LCN and LCN (including SS and MO), the DMN (particularly VIS areas, as well as RSP, MO, and to a lesser extent ACA), TH, LCN-to-SN and MB. These findings, particularly the involvement of the DMN and LCN, are in-line with what has been observed in AD patients [61,62], individuals with mild cognitive impairment (MCI) [63,64], the amyloid-positive but cognitively normal elderly [65], and healthy people of an advanced age [66].

Further, these patterns align (in time and space) with established neurobiological correlates of AD including Aβ-plaques [67] and synapse losses [68] across species. Specifically, the DMN shows *increased* FC in healthy adults where future preferential deposition of Aβ-plaques occur in (older) AD patients [69] in parallel with *decreases* in FC [61]. Further, regions in the DMN (including the RSP or PREC) are among the earliest to show both Aβ-pathology [62] and change in FC in individuals with MCI [64]. Mouse models show Aβ-pathology and synapse density changes in the DMN (RSP and VIS) and LCN (SS and MO), and HF [24]. Mice also show alterations in FC that arise slightly before (at 6-9M) substantial increases in Aβ-pathology (which plateau – in the cortex – within the 8-10M window [24]). Together, these findings hint at a relationship between changes in FC strength that *precede* Aβ-pathology and synapse loss, FC changes which position fMRI as a potentially useful tool for both AD identification and management.

In this regard, AD-associated cognitive deficits are attributable, at least in part, to synaptic failure triggered by Aβ and tau accumulation [70,71]. Targeting a critical link in this cascade (see **Supplementary Discussion**), our group has shown that treatment with BMS-984923 elicits behavioral recovery, normalizes neuronal transcriptomics, prevents synaptic loss (if administered in early stages) and rescues synapse losses (when administered at late stages of the pathology, like in our study) in two mouse models of AD (inclusive of the DKI *App*$^{NL\text{-}G\text{-}F}$*/hMapt*) [27,28]. Here, we conduct the first fMRI investigation of BMS-

984923 treatment effects. To further characterize the therapeutic potential of this drug, we administer to older mice (19-9 vs. 20-22M), after AD-pathology is well established. In BMS-984923 $AD_{treated}$ vs. WT mice (at 22M), we observe normalized FC (**Fig. 5a, S6a**). In $AD_{treated}$ vs. $AD_{vehicle}$ (at 20 or 22M) we observe significant increases in FC (**Fig. 5b**). Although a simple triple-network model is not emergent for these treatment-elicited changes in FC, regions highly involved in the salience network (TH, HY and CP) are detected. Additionally, there is significant overlap with areas implicated in our AD-aging (-ve), WT-aging (+ve), and AD-like (-ve) results (**Fig. 6e**, right).

Using FC in the identified AD-like (-ve) network as a disease measure (**Fig. 7**), the deficits observed in $AD_{vehicle}$ relative to WT mice are fully corrected in $AD_{treated}$ mice at 22 months after 2 months of intervention. Tracking connectivity in this network, or its human ortholog, provides a potential tool to monitor treatment benefit during translational development of this or other AD therapeutics with putative synapse rescuing benefit.

No study is without some limitations, and room for future work. Here, we use anesthesia, the gold standard in rodent-fMRI, to minimize motion and stress [36]. Yet, recent efforts to move the field towards performing experiments in awake mice are underway (see our own work in awake mice[72], and our recent systematic review[73]). As discussed in detail within our review, there is still much we can learn from experiments in anesthetized animals, and from moving methodically towards performing experiments on awake animals. Further, this study does not include a group of $WT_{treated}$ mice. This decision was made based on our previous work which showed no changes in synaptic density or single cell transcriptomics in a $WT_{treated}$ cohort [27]. Finally, although we include equal distributions of both biological sexes, we are not adequately powered for sex-based comparisons. This will be addressed as part of our future work.

In conclusion, we present a comprehensive investigation of the fMRI-FC correlates of AD in an optimized mouse model of the disease across the lifespan (4-22M). A detailed consideration of aging in both healthy-WT mice and their AD-counterparts is included alongside more classic groupwise comparisons. Overall, our findings align well with the existing literature from other mouse models and the human fMRI literature. We observe progressive AD-related dysconnectivity that emerges in known AD-vulnerable areas (sites of Aβ-accumulation, Tauopathy, and synaptic loss). Administration of a synapse-targeting

treatment (BMS-984923) rescues the observed FC deficits in late-stage disease indicating the potential utility of this therapeutic as a synapse *rescuing* treatment and the role neuroimaging with fMRI could play in therapeutic development and patient management.

Methods

All procedures are approved by the Yale Institutional Animal Care and Use Committee (IACUC) and follow the National Institute of Health Guide for the Care and Use of Laboratory Animals. Both biological sexes are included. Mice are group housed on a 12-hour light/dark cycle with *ad libitum* food and water. Cages are individually ventilated as well as temperature and humidity controlled.

Model of Alzheimer's disease

Among available AD models there are amyloid-precursor-protein (App) knock-in (KI) strains[24,25]. Here, we use $App^{NL\text{-}G\text{-}F}$ KI mice where aβ-containing exons from human APP with Swedish, Arctic, and Iberian mutations are included[24]. In addition, mice are crossed with a strain in which the human microtubule-associated protein tau (*MAPT*) locus, with its full sequence and splice sites, replaces the murine locus to generate $App^{NL\text{-}G\text{-}F}$*/hMapt* homozygous double-knock-in animals[24]. The strain has been back-crossed with C57Bl6J for >10 generations, with strain matching confirmed by genetic markers. Male and female AD and wild-type (WT) littermate controls are included.

Dataset overview

A total of N=74 animals are included from across three experiments (**Table 1**). In the first experiment, N=27 animals undergo transverse sinus injections on postnatal day zero (P_0) to induce whole-brain fluorescence. These mice then undergo head-post surgery at 3M and multimodal imaging at 4, 6, and 9M where wide-field calcium (WF-Ca^{2+}) and fMRI data are collected simultaneously[33,74]. The WF-Ca^{2+} imaging data are the subject matter of a separate publication. In the second experiment, N=16 animals undergo head-post surgery at 5 or 8M and unimodal imaging (fMRI-only) at 6 or 9M, respectively. These data are collected to address attrition in the first experiment. In the final experiment, N=30 animals undergo head-post surgery at 19M and unimodal imaging (fMRI-only) at 20 and 22M. Between these imaging sessions, AD mice are split between a treatment (N=11) and vehicle (N=9) subgroup.

Head-implant surgery

At 3M (N=27), 5/8M (N=4/13), or 19M (N=30), all animals undergo a surgical procedure where an in-house built glass head-plate is affixed to the skull. The surgical procedure is based on the design we have described previously[33]. Surgical details are provided in the **Supplementary Material**.

Data acquisition

All mice undergo imaging under anesthesia (free-breathing low-dose isoflurane, 0.5-0.75%, in 50/50 medical air/O_2). The MRI data are acquired on an 11.7T preclinical magnet (Bruker, Billerica, MA), using ParaVision version 6.0.1 software. Body temperature is monitored (Neoptix fiber), maintained with a circulating water bath at 36.6-37°C, and recorded (Spike2, Cambridge Electronic Design Limited, Master-8 A.M.P.I.). Breathing rate is measured using a foam respiration pad (SAM-32, Starr).

Structural MRI data acquisition

At every imaging session, three structural images are acquired for data registration purposes. (1) A multi-spin-multi-echo (MSME) image sharing the same field-of-view (FOV) as the fMRI data. Acquired with a repetition time (TR) of 2500ms and echo time (TE) of 20ms, 28 slices, two averages, and resolution of 0.1×0.1×0.4 mm^3 (10mins and 40sec). (2) A whole-brain isotropic 3D image using a MSME sequence, with 0.2×0.2×0.2mm^3 resolution, TR/TE of 5500/20ms, 78 slices, and 2 averages (11mins and 44sec). (3) A fast-low-angle-shot (FLASH) time-of-flight (TOF) angiogram (FOV, 2.0×1.0×2.5cm^3, covering the cortex), TR/TE of 130/4ms, and resolution of 0.05×0.05×0.05mm^3 (18mins). Of note, the FLASH-TOF was not acquired in the animals that did not undergo multimodal imaging (i.e., animals in experiments 2 and 3).

Functional MRI data acquisition

Data are acquired using a gradient-echo, echo-planar-imaging (GE-EPI) sequence with a TR/TE of 1.8sec/11ms. Data are collected across 25 slices without gaps at 0.31×0.31×0.31mm^3; resulting in near whole-brain coverage. Each run has 334 repetitions, corresponding to 10min of data per run. We acquire 3 runs per session for a total of 30min of data per mouse per imaging session.

Functional MRI preprocessing and registration to common space

Data registration and preprocessing is performed using RABIES (Rodent automated BOLD improvement of EPI sequences) v0.4.8 (https://rabies.readthedocs.io/en/stable/)[34]. All functional and isotropic MSME structural scans (from all imaging sessions and experiments, **Table 1**) are input and preprocessed together. We apply slice time correction, structural and functional inhomogeneity correction N3 (a nonparametric nonuniform intensity normalization)[75,76], and motion correction (ANTS, Advanced normalization tools)[77] in native space. The six-parameters motion estimates are regressed from the timeseries data and used to compute framewise-displacement (FD). Frame scrubbing for motion using a conservative 0.075mm threshold is applied. Cerebrospinal fluid (CSF) and white matter (WM) are also used as nuisance regressors for the final timeseries analyses. Data are smoothed with 0.4 sigma.

The isotropic MSME structural images (one per mouse per session) are non-linearly registered then averaged to create a within-sample template. The within-sample template is non-linearly registered to an out-of-sample template we created from N=162 datasets (collected on the same scanner from N=64 mice from a separate longitudinal study which uses the same isotropic MSME sequence), see **Supplementary Material**. The out-of-sample template is registered to the Allen Atlas reference space CCfv3[37,38]. The preprocessed fMRI data from each mouse at each imaging session are averaged to create a representative mean image that is non-linearly registered to the isotropic structural MSME image acquired during the same imaging session. This procedure minimizes the effects of distortions caused by susceptibility artifacts[78]. Then, three transforms - (1) representative mean fMRI to individual mouse/session isotropic MSME image, (2) individual mouse/session isotropic MSME image to within-dataset template, and (3) within-dataset template to out-of-sample template – are concatenated and applied to the fMRI data. As part of this step, the native resolution of the functional data ($0.31\times0.31\times0.31mm^3$) is resampled to the template resolution ($0.2\times0.2\times0.2mm^3$). The Allen Atlas (which resides in the out-of-sample template space) can then be applied to the fMRI data to compute connectomes. Registration performance is visually inspected.

Exclusion criteria

Of all N=74, N=6 animals and n=2 runs are completely excluded. N=1 for enlarged ventricles, N=1 for a brain tumor, N=2 for anesthesia malfunction (i.e., tubes were improperly connected, N=1 at 4M and N=1

at 6M), and N=2 due to implant detachment (caused by a glass coating that was not present in other surgeries, see **Supplementary Material**). The n=2 excluded scans (n=1 at 6M and n=1 at 9M), were due to image registration failures. More details are given in the **Supplementary Material**. Further, no data are excluded due to a low signal to noise ratio or motion (FD >0.075mm in over 1/3rd of frames per run), or based on recommended quality control metrics obtained from RABIES (*--data diagnosis*)[34].

Connectomes

The 172 ROIs from the Allen Atlas (**Fig. S1**) and MRI template space are shared as part of BioImage Suite (https://bioimagesuiteweb.github.io/alphaapp/connviewer.html?species=mouse#). The ROIs were selected based on the resolution of our fMRI data. To compute connectomes, BOLD signals within each ROI are averaged, and the inter-regional Pearson's correlation computed. Results are computed for each run using data in the out-of-sample template space.

Triple-network model

From the 172-ROI Allen Atlas, we select ROIs that belong to a DMN based on the description by Whitesell and colleagues[41]. Additionally, ROIs belonging to a SN and LCN are selected based on the triple-network model[29,30,79]. Within our template space, these correspond to: DMN [2:3,18:19,28:31, 38:40], SN [2:3, 28:29, 35:37, 59:61, 63, 70:71, 74:75] and LCN [2:11, 41, 62].

Treatment

Drug synthesis, incorporation into diet, feeding, and validation are based on previous work. See summary in **Supplementary Material**.

Statistics

Functional connectomes are z-scored. Descriptive statistics are given as mean differences and 25/75th percentiles unless stated otherwise, and graphically represented as box plots (MATLAB, *boxplot*). Statistical significance tests are computed in MATLAB (R2021bV5). Differences between connectomes are tested using a two-sample t-test (MATLAB, ttest2), and confirmed with a permutation-based test (×1,000 iterations) where data from the groups being compared are randomly shuffled and the comparison repeated. The statistical threshold for significance is set to $p<0.05$, two-tailed. Correction for

multiple comparison is performed with the Benjamini-Hochberg test. The test shows that the true group labels lead to significantly more different edges than random labelling. For the 22M timepoint, a one-way ANOVA (MATLAB, *anova1*) is used to compare the treatment effect on the genotype, first and a two-sample t-test is used after to compare each two groups ($WT_{vehicle}$ vs. $AD_{vehicle}$, $WT_{vehicle}$ vs $AD_{treated}$, and $AD_{vehicle}$ vs $AD_{treated}$), results reported as above. The overlap of the maps used to create aging networks, and genotype networks are assessed with Jaccard similarity test and compared to a null distribution (×1,000 iterations) to confirm the meaningfulness of the significant overlap found. Finally, the over/under enrichment of the triple-network model with the data-derived networks is calculated with Fisher's exact test as well as permutation testing (as described above, ×1,000 iterations).

Acknowledgments

Drs. Joel Greenwood, Omer Mano, and Paul Shamble from the Neurotechnology Core of the Yale Kavli Institute for Neuroscience for their technological expertise. Drs. Michael Crair and Ali Hamodi for help with optimizing and implementing transverse sinus injection experiments. Dr. Yonghyun Ha for his technical expertise and coil mending abilities. Dr. Corey Horien for critical discussion and coding advice. Kristin DeLuca for mouse husbandry. This work was supported by the Yale Alzheimer's Disease Research Center P30AG066508 (S.M.S. & E.M.R.L.) and the Wu Tsai Institute at Yale (S.M.S. & E.M.R.L.), plus NIH projects R21AG075778-01 (E.M.R.L.), RF1NS130069 (E.M.R.L. & S.M.S.), R01AG034924 (S.M.S.) and RF1AG070926 (S.M.S.).

Author contributions

FM, SMS, and EMRL designed the study. FM carried out the surgical procedures, data acquisition, analyses and wrote the manuscript. GDG, DO, XS, and XP contributed code. AQ and JO implemented the skull stripping algorithm. BM and AO helped with animal and tissue handling. MC supervised GDG and edited the manuscript. SMS and EMRL supervised the study.

Declaration of interests

S.M.S. is a Founder, Consultant, Equity Holder and Director of Allyx Therapeutics seeking to develop mGluR5-directed therapies for Alzheimer's and Parkinson's Disease.

Data sharing

Upon reasonable request to the corresponding authors.

References

1. Kim J, Jeong M, Stiles WR, Choi HS. Neuroimaging Modalities in Alzheimer's Disease: Diagnosis and Clinical Features. *Int J Mol Sci*. May 28 2022;23(11)doi:10.3390/ijms23116079
2. Marquez F, Yassa MA. Neuroimaging Biomarkers for Alzheimer's Disease. *Mol Neurodegener*. Jun 7 2019;14(1):21. doi:10.1186/s13024-019-0325-5
3. Wang X, Huang W, Su L, et al. Neuroimaging advances regarding subjective cognitive decline in preclinical Alzheimer's disease. *Mol Neurodegener*. Sep 22 2020;15(1):55. doi:10.1186/s13024-020-00395-3
4. Chetelat G. Multimodal Neuroimaging in Alzheimer's Disease: Early Diagnosis, Physiopathological Mechanisms, and Impact of Lifestyle. *J Alzheimers Dis*. 2018;64(s1):S199-S211. doi:10.3233/JAD-179920
5. Sheline YI, Morris JC, Snyder AZ, et al. APOE4 allele disrupts resting state fMRI connectivity in the absence of amyloid plaques or decreased CSF Abeta42. *J Neurosci*. Dec 15 2010;30(50):17035-40. doi:10.1523/JNEUROSCI.3987-10.2010
6. Morris JC, Storandt M, McKeel DW, Jr., et al. Cerebral amyloid deposition and diffuse plaques in "normal" aging: Evidence for presymptomatic and very mild Alzheimer's disease. *Neurology*. Mar 1996;46(3):707-19. doi:10.1212/wnl.46.3.707
7. Buckner RL, Andrews-Hanna JR, Schacter DL. The brain's default network: anatomy, function, and relevance to disease. *Ann N Y Acad Sci*. Mar 2008;1124:1-38. doi:10.1196/annals.1440.011
8. Scheff SW, Price DA, Schmitt FA, Mufson EJ. Hippocampal synaptic loss in early Alzheimer's disease and mild cognitive impairment. *Neurobiol Aging*. Oct 2006;27(10):1372-84. doi:10.1016/j.neurobiolaging.2005.09.012
9. Terry RD, Masliah E, Salmon DP, et al. Physical basis of cognitive alterations in Alzheimer's disease: synapse loss is the major correlate of cognitive impairment. *Ann Neurol*. Oct 1991;30(4):572-80. doi:10.1002/ana.410300410
10. DeKosky ST, Scheff SW. Synapse loss in frontal cortex biopsies in Alzheimer's disease: correlation with cognitive severity. *Ann Neurol*. May 1990;27(5):457-64. doi:10.1002/ana.410270502
11. Sze CI, Troncoso JC, Kawas C, Mouton P, Price DL, Martin LJ. Loss of the presynaptic vesicle protein synaptophysin in hippocampus correlates with cognitive decline in Alzheimer disease. *J Neuropathol Exp Neurol*. Aug 1997;56(8):933-44. doi:10.1097/00005072-199708000-00011
12. Morrison JH, Baxter MG. The ageing cortical synapse: hallmarks and implications for cognitive decline. *Nat Rev Neurosci*. Mar 7 2012;13(4):240-50. doi:10.1038/nrn3200
13. Mandino F, Yeow LY, Bi RZ, et al. The lateral entorhinal cortex is a hub for local and global dysfunction in early Alzheimer's disease states. *J Cerebr Blood F Met*. Apr 25 2022;doi:Artn 0271678x221082016
10.1177/0271678x221082016
14. Grandjean J, Derungs R, Kulic L, et al. Complex interplay between brain function and structure during cerebral amyloidosis in APP transgenic mouse strains revealed by multi-parametric MRI comparison. *Neuroimage*. Jul 1 2016;134:1-11. doi:10.1016/j.neuroimage.2016.03.042
15. Shah D, Jonckers E, Praet J, et al. Resting state FMRI reveals diminished functional connectivity in a mouse model of amyloidosis. *PLoS One*. 2013;8(12):e84241. doi:10.1371/journal.pone.0084241
16. Mandino F, Cerri DH, Garin CM, et al. Animal Functional Magnetic Resonance Imaging: Trends and Path Toward Standardization. *Front Neuroinform*. Jan 22 2020;13doi:ARTN 78
10.3389/fninf.2019.00078
17. Markicevic M, Savvateev I, Grimm C, Zerbi V. Emerging imaging methods to study whole-brain function in rodent models. *Transl Psychiatry*. Sep 4 2021;11(1):457. doi:10.1038/s41398-021-01575-5
18. Gorges M, Roselli F, Muller HP, Ludolph AC, Rasche V, Kassubek J. Functional Connectivity Mapping in the Animal Model: Principles and Applications of Resting-State fMRI. *Front Neurol*. 2017;8:200. doi:10.3389/fneur.2017.00200
19. Zerbi V, Grandjean J, Rudin M, Wenderoth N. Mapping the mouse brain with rs-fMRI: An optimized pipeline for functional network identification. *Neuroimage*. Dec 2015;123:11-21. doi:10.1016/j.neuroimage.2015.07.090

20. Grandjean J, Schroeter A, Batata I, Rudin M. Optimization of anesthesia protocol for resting-state fMRI in mice based on differential effects of anesthetics on functional connectivity patterns. *Neuroimage*. Nov 15 2014;102:838-847. doi:10.1016/j.neuroimage.2014.08.043
21. Xu N, LaGrow TJ, Anumba N, et al. Functional Connectivity of the Brain Across Rodents and Humans. *Front Neurosci*. 2022;16:816331. doi:10.3389/fnins.2022.816331
22. Gozzi A, Zerbi V. Modeling Brain Dysconnectivity in Rodents. *Biol Psychiatry*. Mar 1 2023;93(5):419-429. doi:10.1016/j.biopsych.2022.09.008
23. Sharma H, Chang KA, Hulme J, An SSA. Mammalian Models in Alzheimer's Research: An Update. *Cells*. Oct 16 2023;12(20)doi:10.3390/cells12202459
24. Saito T, Matsuba Y, Mihira N, et al. Single App knock-in mouse models of Alzheimer's disease. *Nat Neurosci*. May 2014;17(5):661-3. doi:10.1038/nn.3697
25. Saito T, Mihira N, Matsuba Y, et al. Humanization of the entire murine Mapt gene provides a murine model of pathological human tau propagation. *J Biol Chem*. Aug 23 2019;294(34):12754-12765. doi:10.1074/jbc.RA119.009487
26. Dutta S, Sengupta P. Men and mice: Relating their ages. *Life Sci*. May 1 2016;152:244-8. doi:10.1016/j.lfs.2015.10.025
27. Spurrier J, Nicholson L, Fang XT, et al. Reversal of synapse loss in Alzheimer mouse models by targeting mGluR5 to prevent synaptic tagging by C1Q. *Sci Transl Med*. Jun 2022;14(647):eabi8593. doi:10.1126/scitranslmed.abi8593
28. Haas LT, Salazar SV, Smith LM, et al. Silent Allosteric Modulation of mGluR5 Maintains Glutamate Signaling while Rescuing Alzheimer's Mouse Phenotypes. *Cell Rep*. Jul 5 2017;20(1):76-88. doi:10.1016/j.celrep.2017.06.023
29. Menon V. Large-scale brain networks and psychopathology: a unifying triple network model. *Trends Cogn Sci*. Oct 2011;15(10):483-506. doi:10.1016/j.tics.2011.08.003
30. Mandino F, Vrooman RM, Foo HE, et al. A triple-network organization for the mouse brain. *Mol Psychiatr*. Feb 2022;27(2):865-872. doi:10.1038/s41380-021-01298-5
31. Vafaii H, Mandino F, Desrosiers-Gregoire G, et al. Multimodal measures of spontaneous brain activity reveal both common and divergent patterns of cortical functional organization. 2023;
32. O'Connor D, Mandino F, Shen X, et al. Functional network properties derived from wide-field calcium imaging differ with wakefulness and across cell type. *NeuroImage*. 2022;264:119735.
33. Lake EMR, Ge X, Shen X, et al. Simultaneous cortex-wide fluorescence Ca(2+) imaging and whole-brain fMRI. *Nat Methods*. Jul 2020;18(7):835. doi:10.1038/s41592-021-01217-0
34. Desrosiers-Gregoire G, Devenyi GA, Grandjean J, Chakravarty MM. Rodent Automated Bold Improvement of EPI Sequences (RABIES): A standardized image processing and data quality platform for rodent fMRI. *bioRxiv*. 2022:2022.08. 20.504597.
35. Grandjean J, Desrosiers-Gregoire G, Anckaerts C, et al. A consensus protocol for functional connectivity analysis in the rat brain. *Nature neuroscience*. 2023;26(4):673-681.
36. Grandjean J, Canella C, Anckaerts C, et al. Common functional networks in the mouse brain revealed by multi-centre resting-state fMRI analysis. *Neuroimage*. 2020;205:116278.
37. Atlas AMB. Allen institute for brain science. *Available online at: mouse brain-map org*. 2004;
38. Wang Q, Ding SL, Li Y, et al. The Allen Mouse Brain Common Coordinate Framework: A 3D Reference Atlas. *Cell*. May 14 2020;181(4):936-953 e20. doi:10.1016/j.cell.2020.04.007
39. Bondi MW, Houston WS, Salmon DP, et al. Neuropsychological deficits associated with Alzheimer's disease in the very-old: discrepancies in raw vs. standardized scores. *J Int Neuropsychol Soc*. Jul 2003;9(5):783-95. doi:10.1017/S1355617703950119
40. Betzel RF, Byrge L, He Y, Goni J, Zuo XN, Sporns O. Changes in structural and functional connectivity among resting-state networks across the human lifespan. *Neuroimage*. Nov 15 2014;102 Pt 2:345-57. doi:10.1016/j.neuroimage.2014.07.067
41. Whitesell JD, Liska A, Coletta L, et al. Regional, Layer, and Cell-Type-Specific Connectivity of the Mouse Default Mode Network. *Neuron*. Feb 3 2021;109(3)doi:10.1016/j.neuron.2020.11.011
42. Yarkoni T, Poldrack RA, Nichols TE, Van Essen DC, Wager TD. Large-scale automated synthesis of human functional neuroimaging data. *Nat Methods*. Jun 26 2011;8(8):665-70. doi:10.1038/nmeth.1635
43. Zhang H, Wu L, Pchitskaya E, et al. Neuronal Store-Operated Calcium Entry and Mushroom Spine Loss in Amyloid Precursor Protein Knock-In Mouse Model of Alzheimer's Disease. *J Neurosci*. Sep 30 2015;35(39):13275-86. doi:10.1523/JNEUROSCI.1034-15.2015

44. Vasilkovska T, Adhikari MH, Van Audekerke J, et al. Resting-state fMRI reveals longitudinal alterations in brain network connectivity in the zQ175DN mouse model of Huntington's disease. *Neurobiol Dis*. Jun 1 2023;181:106095. doi:10.1016/j.nbd.2023.106095
45. Egimendia A, Minassian A, Diedenhofen M, Wiedermann D, Ramos-Cabrer P, Hoehn M. Aging Reduces the Functional Brain Networks Strength-a Resting State fMRI Study of Healthy Mouse Brain. *Front Aging Neurosci*. 2019;11:277. doi:10.3389/fnagi.2019.00277
46. Albertson AJ, Landsness EC, Tang MJ, et al. Normal aging in mice is associated with a global reduction in cortical spectral power and network-specific declines in functional connectivity. *Neuroimage*. Aug 15 2022;257:119287. doi:10.1016/j.neuroimage.2022.119287
47. Mak LE, Minuzzi L, MacQueen G, Hall G, Kennedy SH, Milev R. The Default Mode Network in Healthy Individuals: A Systematic Review and Meta-Analysis. *Brain Connect*. Feb 2017;7(1):25-33. doi:10.1089/brain.2016.0438
48. Staffaroni AM, Brown JA, Casaletto KB, et al. The Longitudinal Trajectory of Default Mode Network Connectivity in Healthy Older Adults Varies As a Function of Age and Is Associated with Changes in Episodic Memory and Processing Speed. *J Neurosci*. Mar 14 2018;38(11):2809-2817. doi:10.1523/JNEUROSCI.3067-17.2018
49. Bo J, Lee CM, Kwak Y, et al. Lifespan differences in cortico-striatal resting state connectivity. *Brain Connect*. Apr 2014;4(3):166-80. doi:10.1089/brain.2013.0155
50. Jolles DD, van Buchem MA, Crone EA, Rombouts SA. A comprehensive study of whole-brain functional connectivity in children and young adults. *Cereb Cortex*. Feb 2011;21(2):385-91. doi:10.1093/cercor/bhq104
51. Li Z, Petersen IT, Wang L, Radua J, Yang G, Liu X. Inverted U-shaped brain development of cognitive control across the human lifespan. *bioRxiv*. Aug 21 2023;doi:10.1101/2023.08.20.554018
52. McDonough IM, Nolin SA, Visscher KM. 25 years of neurocognitive aging theories: What have we learned? *Front Aging Neurosci*. 2022;14:1002096. doi:10.3389/fnagi.2022.1002096
53. Sala-Llonch R, Bartres-Faz D, Junque C. Reorganization of brain networks in aging: a review of functional connectivity studies. *Front Psychol*. 2015;6:663. doi:10.3389/fpsyg.2015.00663
54. Vafaii H, Mandino F, Desrosiers-Gregoire G, et al. Multimodal measures of spontaneous brain activity reveal both common and divergent patterns of cortical functional organization. *Res Sq*. Apr 26 2023;doi:10.21203/rs.3.rs-2823802/v1
55. O'Connor D, Mandino F, Shen X, et al. Functional network properties derived from wide-field calcium imaging differ with wakefulness and across cell type. *NeuroImage*. 2022;264:119735.
56. Shah D, Praet J, Latif Hernandez A, et al. Early pathologic amyloid induces hypersynchrony of BOLD resting-state networks in transgenic mice and provides an early therapeutic window before amyloid plaque deposition. *Alzheimers Dement*. Sep 2016;12(9):964-976. doi:10.1016/j.jalz.2016.03.010
57. Zerbi V, Wiesmann M, Emmerzaal TL, et al. Resting-state functional connectivity changes in aging apoE4 and apoE-KO mice. *J Neurosci*. Oct 15 2014;34(42):13963-75. doi:10.1523/JNEUROSCI.0684-14.2014
58. Damoiseaux JS, Beckmann CF, Arigita EJ, et al. Reduced resting-state brain activity in the "default network" in normal aging. *Cereb Cortex*. Aug 2008;18(8):1856-64. doi:10.1093/cercor/bhm207
59. Onoda K, Ishihara M, Yamaguchi S. Decreased functional connectivity by aging is associated with cognitive decline. *J Cogn Neurosci*. Nov 2012;24(11):2186-98. doi:10.1162/jocn_a_00269
60. Sasaguri H, Hashimoto S, Watamura N, et al. Recent Advances in the Modeling of Alzheimer's Disease. *Front Neurosci*. 2022;16:807473. doi:10.3389/fnins.2022.807473
61. Greicius MD, Srivastava G, Reiss AL, Menon V. Default-mode network activity distinguishes Alzheimer's disease from healthy aging: evidence from functional MRI. *Proc Natl Acad Sci U S A*. Mar 30 2004;101(13):4637-42. doi:10.1073/pnas.0308627101
62. Sheline YI, Raichle ME. Resting state functional connectivity in preclinical Alzheimer's disease. *Biol Psychiatry*. Sep 1 2013;74(5):340-7. doi:10.1016/j.biopsych.2012.11.028
63. Wang J, Zuo X, Dai Z, et al. Disrupted functional brain connectome in individuals at risk for Alzheimer's disease. *Biol Psychiatry*. Mar 1 2013;73(5):472-81. doi:10.1016/j.biopsych.2012.03.026
64. Vann SD, Aggleton JP, Maguire EA. What does the retrosplenial cortex do? *Nature Reviews Neuroscience*. 2009/11/01 2009;10(11):792-802. doi:10.1038/nrn2733

65. Sheline YI, Raichle ME, Snyder AZ, et al. Amyloid plaques disrupt resting state default mode network connectivity in cognitively normal elderly. *Biol Psychiatry*. Mar 15 2010;67(6):584-7. doi:10.1016/j.biopsych.2009.08.024
66. Andrews-Hanna JR, Snyder AZ, Vincent JL, et al. Disruption of large-scale brain systems in advanced aging. *Neuron*. Dec 6 2007;56(5):924-35. doi:10.1016/j.neuron.2007.10.038
67. Hampel H, Hu Y, Hardy J, et al. The amyloid-beta pathway in Alzheimer's disease: a plain language summary. *Neurodegener Dis Manag*. Jun 2023;13(3):141-149. doi:10.2217/nmt-2022-0037
68. Zhang J, Wang J, Xu X, et al. In vivo synaptic density loss correlates with impaired functional and related structural connectivity in Alzheimer's disease. *J Cereb Blood Flow Metab*. Jun 2023;43(6):977-988. doi:10.1177/0271678X231153730
69. Buckner RL, Snyder AZ, Shannon BJ, et al. Molecular, structural, and functional characterization of Alzheimer's disease: evidence for a relationship between default activity, amyloid, and memory. *J Neurosci*. Aug 24 2005;25(34):7709-17. doi:10.1523/JNEUROSCI.2177-05.2005
70. Selkoe DJ. Alzheimer's disease is a synaptic failure. *Science*. Oct 25 2002;298(5594):789-91. doi:10.1126/science.1074069
71. Brier MR, Thomas JB, Ances BM. Network dysfunction in Alzheimer's disease: refining the disconnection hypothesis. *Brain Connect*. Jun 2014;4(5):299-311. doi:10.1089/brain.2014.0236
72. Mandino F, Shen X, O'Connor D, et al. Longitudinal simultaneous cortex-wide Ca2+ imaging and whole-brain functional magnetic resonance imaging in awake mice. SAGE PUBLICATIONS INC 2455 TELLER RD, THOUSAND OAKS, CA 91320 USA; 2022:75-75.
73. Mandino F. Where do we stand on fMRI in awake mice? Systematic Review. *Cerebral cortex*. Dec 2023.
74. Vafaii H, Mandino F, Desrosiers-Gregoire G, et al. Functional network organization of the mouse cortex determined by wide-field fluorescence imaging shares some—but not all—properties revealed with simultaneous fMRI-BOLD. *bioRxiv*. 2022:2022.12. 13.520297.
75. Manjon JV, Coupe P, Marti-Bonmati L, Collins DL, Robles M. Adaptive Non-Local Means Denoising of MR Images With Spatially Varying Noise Levels. *J Magn Reson Imaging*. Jan 2010;31(1):192-203. doi:10.1002/jmri.22003
76. Sled JG, Zijdenbos AP, Evans AC. A nonparametric method for automatic correction of intensity nonuniformity in MRI data. *Ieee T Med Imaging*. Feb 1998;17(1):87-97. doi:Doi 10.1109/42.668698
77. Avants BB, Tustison NJ, Song G, Cook PA, Klein A, Gee JC. A reproducible evaluation of ANTs similarity metric performance in brain image registration. *Neuroimage*. Feb 1 2011;54(3):2033-44. doi:10.1016/j.neuroimage.2010.09.025
78. Wang SJ, Peterson DJ, Gatenby JC, Li WB, Grabowski TJ, Madhyastha TM. Evaluation of Field Map and Nonlinear Registration Methods for Correction of Susceptibility Artifacts in Diffusion MRI. *Front Neuroinform*. Feb 21 2017;11doi:ARTN 17
10.3389/fninf.2017.00017
79. Menon V. The Triple Network Model, Insight, and Large-Scale Brain Organization in Autism. *Biol Psychiatry*. Aug 15 2018;84(4):236-238. doi:10.1016/j.biopsych.2018.06.012

Tables and Figures

Table 1| Overview of datasets

	Experiment 1				Experiment 2				Experiment 3			
	♂		♀		♂		♀		♂		♀	
Procedure	**WT**	**AD**	**WT**	**AD**	**WT**	**AD**	**WT**	**AD**	**WT**	**AD**	**WT**	**AD**
Transverse sinus injection	5	8	6	8								
Head-plate at 3M	5	8	6	8								
Head-plate at 5M					-	-	-	4				
Head-plate at 8M					6	4	2	1				
Head-plate at 19M									5	12	5	8
Multimodal imaging at 4M	5	7+1$	5+1$	8								
Multimodal imaging at 6M	5	5+1$	5	3								
Multimodal imaging at 9M	-	2	2	4								
Unimodal* imaging at 6M								4				
Unimodal* imaging at 9M					6	4	2	1				
Unimodal* imaging at 20M									5	12	3	7+1$
Allocated to treatment									-	5	-	4
Unimodal* imaging at 22M									5	6/5†	0	3/4†

* Unimodal is always MRI-only
$ excluded
† Vehicle/drug-treated
Abbreviations: wild-type (WT), double knock in (AD), months of age (M).

Table 2| Change in FC strength with age in healthy mice

Age	This study	Egimendia	Vasilkovska	Albertson*
2-4M	Baseline	Baseline	Baseline	Baseline
4-6M	•	•		
6-8M			↑	
8-10M	↑	↑		
10-12M			↓	
12-14M		↓		
14-16M				
16-18M				↓
18-20M	↑			
20-22M	↓			

* Optical imaging of Thy-1-GCaMP6f mice.

Table 3| Brain areas showing changes in FC strength with age in WT-mice

Network/Region	This study	Egimendia	Vasilkovska	Albertson*
DMN	•	•	•	•
RSP†	•	(part of DMN)	•	•
VIS†	•		•	•
MO†	•	•		•
AUD	(**Fig. 6d**)		•	•
ACA†	•		•	•
SS†	•	•		
LCN	•			
HY	•			
TH†	•			
ACB†	•			
MB	•			
PTL‡				•

* Optical imaging cannot access subsurface areas.
† Areas in our Neurosynth analysis (**Fig. S3**).
‡ PTL: Posterior parietal association area [46].
Refer to **Fig. S1** for abbreviations.

Table 4| Brain areas showing changes in FC strength across comparisons in this study

Network/Region		WT-Aging	AD-Aging	WT vs. AD	Shared (Fig. 6)
DMN:		↑ (+ve); ↓ (-ve)	↑ (+ve); ↓ (-ve)	•	★
VIS†		↑ (+ve)	↑ (-ve)	↑ (-ve)	★
RSP†‡ (PREC)		↑ (+ve)	•	↑ (-ve)	★
MO†		↑ (+ve)	•	↑ (-ve)	★
ACA†‡		↑ (+ve)	•	↑ (-ve)	•
LCN:		↑ (+ve)	↓ (-ve)	↑ (-ve)	★
SS†		↑ (+ve)	•	↑ (-ve)	★
TeA		•	•	↑ (-ve)	•
MO†		↑ (+ve)	•	↑ (-ve)	★
SN:		•	•	•	•
HY		↑ (+ve)	•	•	•
TH†		↑ (+ve)	↑ (-ve)	↑ (-ve)	•
INS†‡		•	↑ (-ve)	•	•
MO†		↑ (+ve)	•	↑ (-ve)	★
ACA†‡		↑ (+ve)	•	↑ (-ve)	•
DMN-LCN		↑ (+ve); ↓ (-ve)	↑ (+ve); ↓ (-ve)	↑ (-ve)	★
DMN-SN		↑ (+ve)	↑ (+ve)	•	•
LCN-SN		↑ (+ve)	•	↑ (-ve)	★
Other	MB	↑ (+ve)	•	↑ (-ve)	•
	ECT	•	↑ (-ve)	•	•
	PERI	•	↑ (-ve)	•	•
	HF†	•	↑ (-ve)	↑ (-ve)	•
	CP	•	↑ (-ve)	•	•
	PIR	•	↑ (-ve)	•	•
	PPA	•	•	↑ (-ve)	•
	ACB†	↑ (+ve)	•	•	•
	ENT	•	•	↑ (-ve)	•
	HF‡	•	•	↑ (-ve)	•
	AUD	•	•	•	★
	AA	•	•	•	★

ACB: Nucleus accumbens, ENT: entorhinal cortex.
† Neurosynth results for 'Age' (**Fig. S3**).
‡ Neurosynth results for 'Alzheimer' (**Fig. S3**).
PREC: precuneus (human) to RSP (mouse).
Refer to **Fig. S1** for abbreviations.

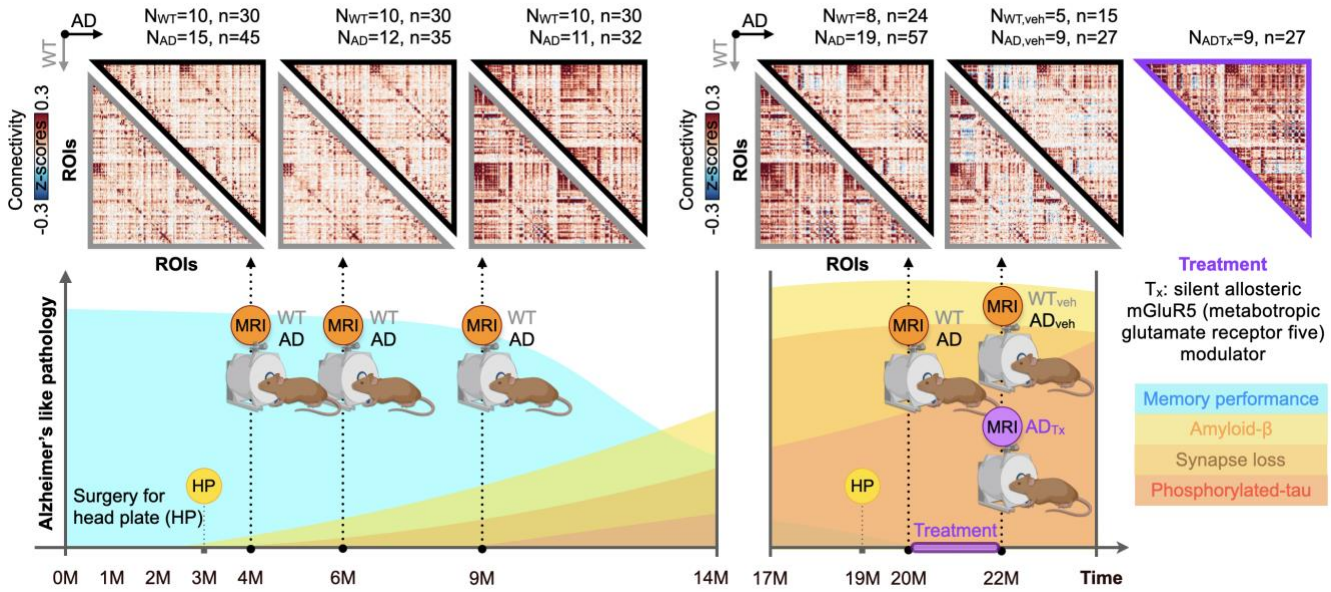

Fig. 1| Schematic of AD-like pathology and study overview. Based on previous work in this AD-model[24,25,27], the approximate trajectory of AD-like pathology is illustrated on the timeline in warm colors: β-amyloid accumulation (yellow), synapse loss (orange) and phosphorylated-tau accumulation (red). Decreasing performance on memory tests (e.g., Y- maze test[24]) is illustrated in blue. Imaging timepoints (MRI, orange) are indicated by black dotted arrows. A month prior to the first imaging timepoint (in each group, **Table 1**), all mice undergo a minimally invasive surgical procedure [33] where a head-plate (HP) is affixed to the skull to reduce susceptibility artifacts and motion (HP, yellow). The treatment (Tx) period is indicated on the timeline (purple). Average Z-scored connectomes for each group at each timepoint are shown above the timeline. Data from WT mice are outlined in grey (lower left). Data from AD (and $AD_{vehicle}$) groups are outlined in black (upper right). Data from the $AD_{treated}$ group (at 22M) are outlined in purple. The number of mice ('N') and runs ('n') are indicated above each connectome. Animal breakdown: 4M: N_{WT}=5/5 M/F;N_{AD}=7/8 M/F; 6M: N_{WT}= 5/5 M/F; N_{AD}=5/7 M/F; 9M: N_{WT}=6/4 M/F; N_{AD}=6/5 M/F; 20M: N_{WT}=5/3 M/F; N_{AD}=12/7 M/F; 22M: N_{WT}=5/0 M/F; N_{ADveh}=6/3 M/F; N_{ADTx}=5/4 M/F.

a. Changes in FC strength with age in WT mice across the lifespan

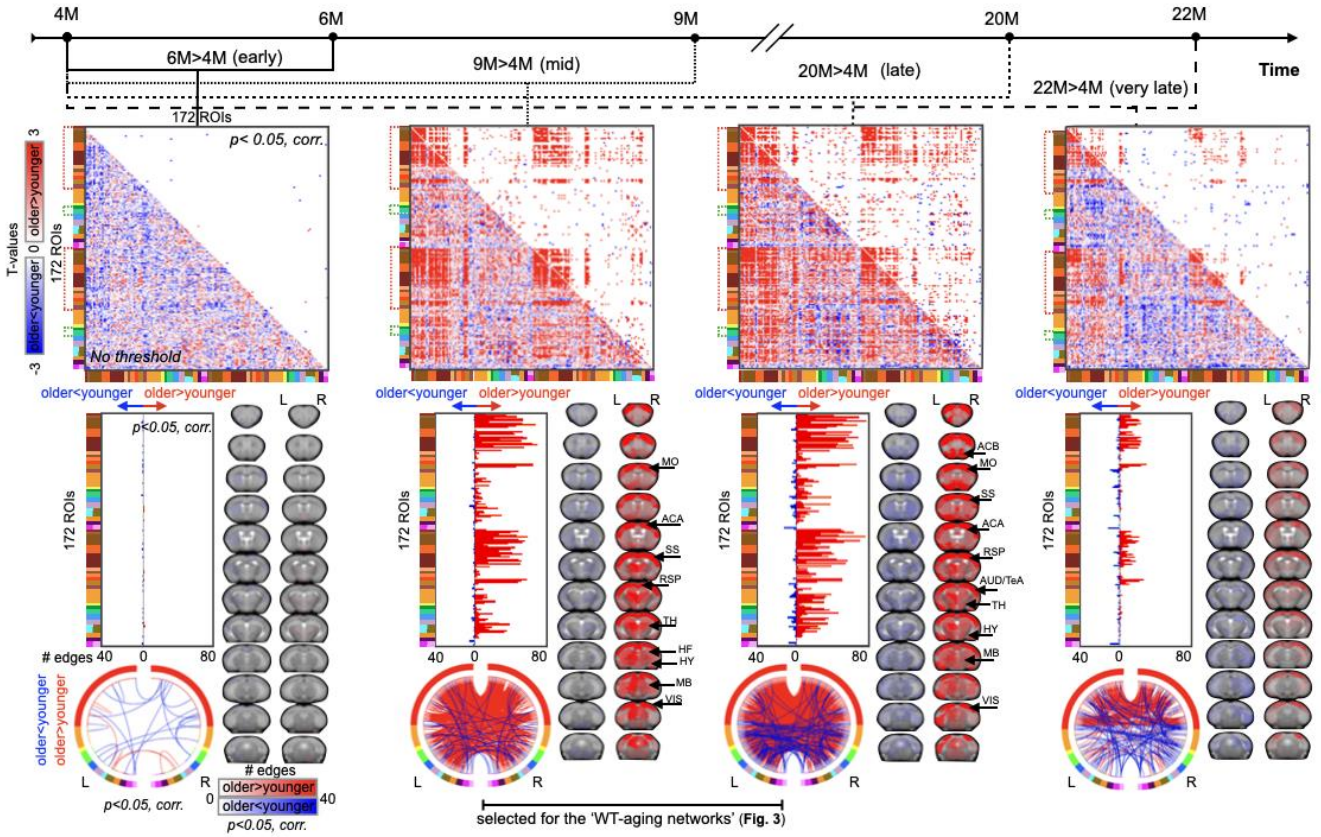

b. Changes in FC strength with age in AD mice across the lifespan

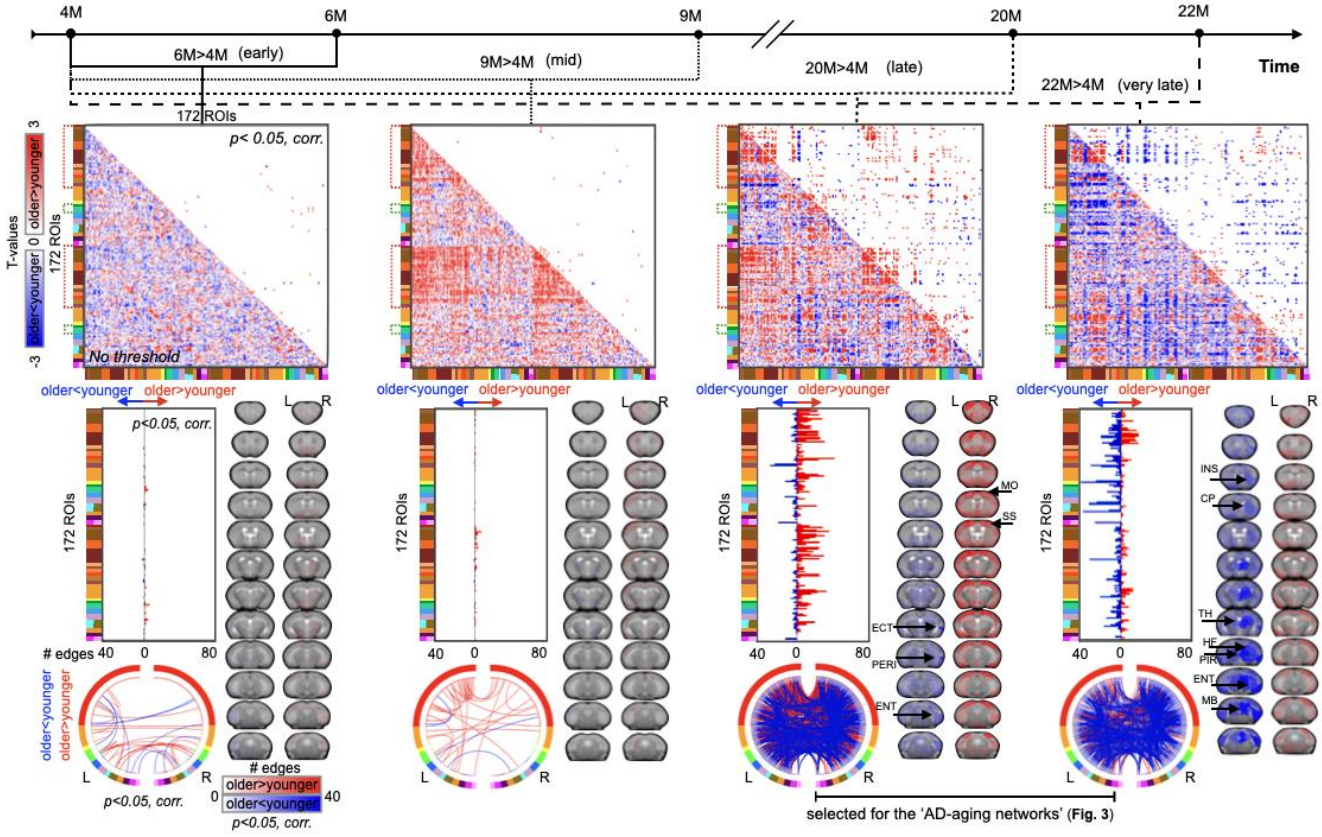

Caption appears on the next page.

Fig. 2| WT and AD follow distinct trajectories of age-related changes in functional brain organization. Two-sample t-tests are applied to uncover age-related changes in FC strength within WT and AD mice (**a.**, and **b.**, respectively). In both groups (WT and AD), the earliest timepoint (4M) is used as a baseline for the four subsequent imaging sessions. Thus, four stages of 'aging' are captured: early (6M vs. 4M), mid (9M vs. 4M), late (20M vs. 4M) and very late (22M vs. 4M). For connectomes, T-test results are displayed without (bottom half), and with (top half) a statistical threshold (corrected, $p < 0.05$). All other displays, vertical histograms of node degree, circle plots and node degree maps, results are shown after the statistical thresholds have been applied. For the brain region labels (rainbow) color-scale, see **Fig. S1**. Positive t-values (red) indicate greater FC strength in older vs. younger mice. Negative values (blue) indicate the opposite. Node degree maps are displayed on anatomical reference images (greyscale). Clear and distinct aging effects are observed in both groups. The WT group shows an overall increase in FC strength in older vs. younger mice which emerges at 9M, persists at 20M, and shows some evidence of waning at 22M. Conversely, the AD group shows an overall decrease in FC strength in older vs. younger mice which emerges at 20M and persists until 22M. As a data reduction strategy, we summarize these data at the indicated timepoints for each group (**Fig. 3**).

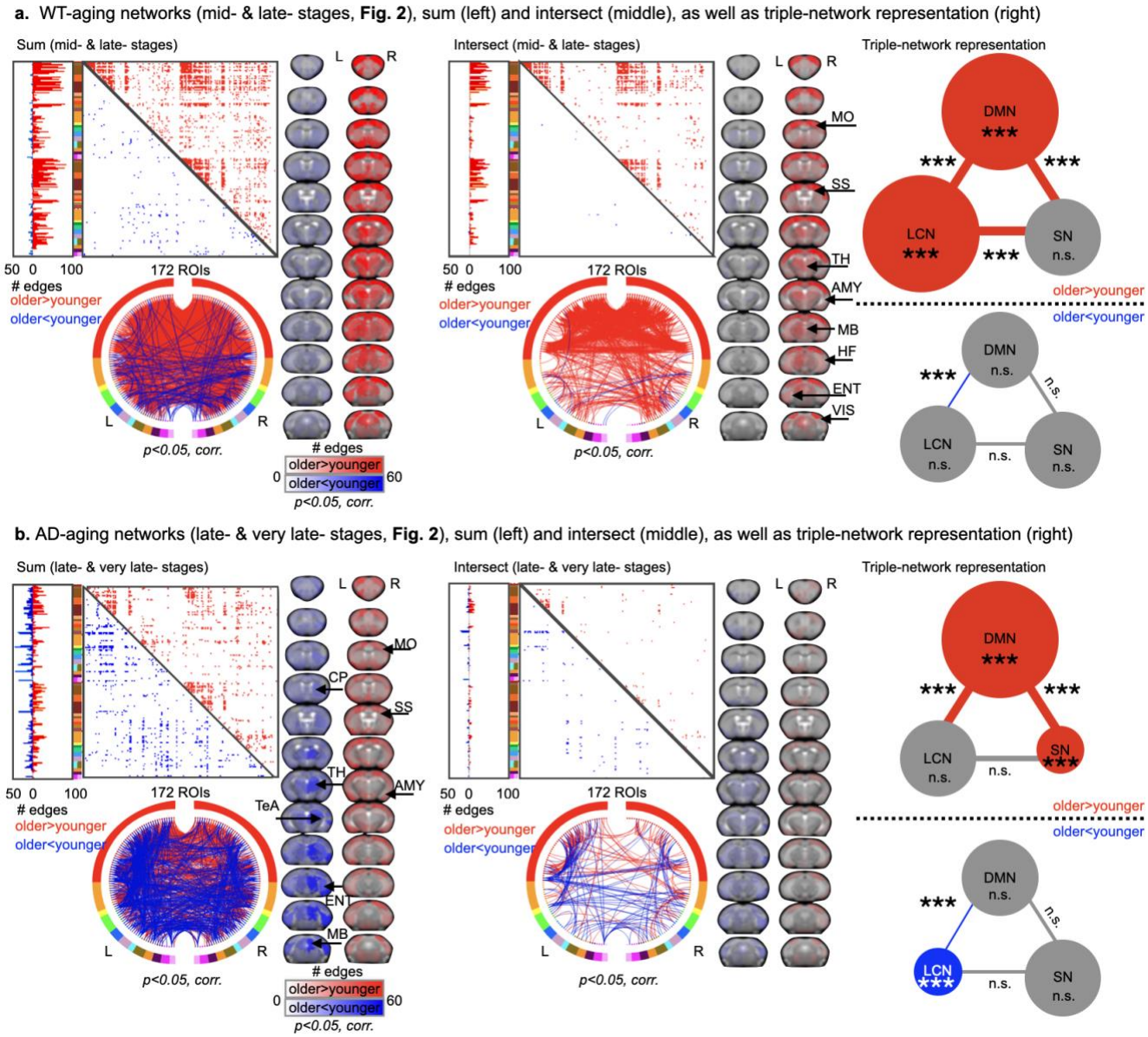

Fig. 3| Summaries of data-derived WT- and AD-aging networks. We consider both the sum (all edges across two stages) and intersect (common edges across two stages) as a comprehensive (sum) and stringent (intersect) definition of our data-driven aging networks (left and middle panels respectively, **a.** and **b.**). Edges at chosen stages (**Fig. 2**) are highly overlapping (difference from null distribution, p<0.001) for both WT (**a.**) and AD (**b.**) groups. Aging networks are displayed as connectomes (172 x 172 ROIs, see **Fig. S1**). Greater FC in older relative to younger mice is shown in red (upper right in connectomes). Greater FC in younger relative to older mice is shown in blue (lower left in connectomes). Data are also shown as vertical histograms of node degree, circle plots, and node degree maps displayed on anatomical reference images (greyscale) in left and middle panels (**a.** and **b.**). All results have a statistical threshold (corrected, p<0.05) applied. Fisher's exact test (MATLAB) is used to assess (under) enrichment for edges within data-derived networks and the triple-network model: DMN, LCN, and SN, as well as their inter-network pairs (corrected, permutation test x1,000 iterations). These results are depicted using ball-and-stick diagrams (right panel). An enlarged ball indicates enrichment (e.g., **a.** WT-aging DMN, older>younger), whereas a shrunken ball indicates under-enrichment (e.g., **a.** WT-aging SN, older>younger). Balls and sticks showing no (under) enrichment are drawn in grey (n.s.) whereas (under) enrichment is indicated by color (red for older>younger, and blue for older<younger). Significance is displayed as * for p<0.05, ** for p<0.01 and *** for p<0.001. Equivalent findings are uncovered for triple network representation when we use the sum or intersect definition.

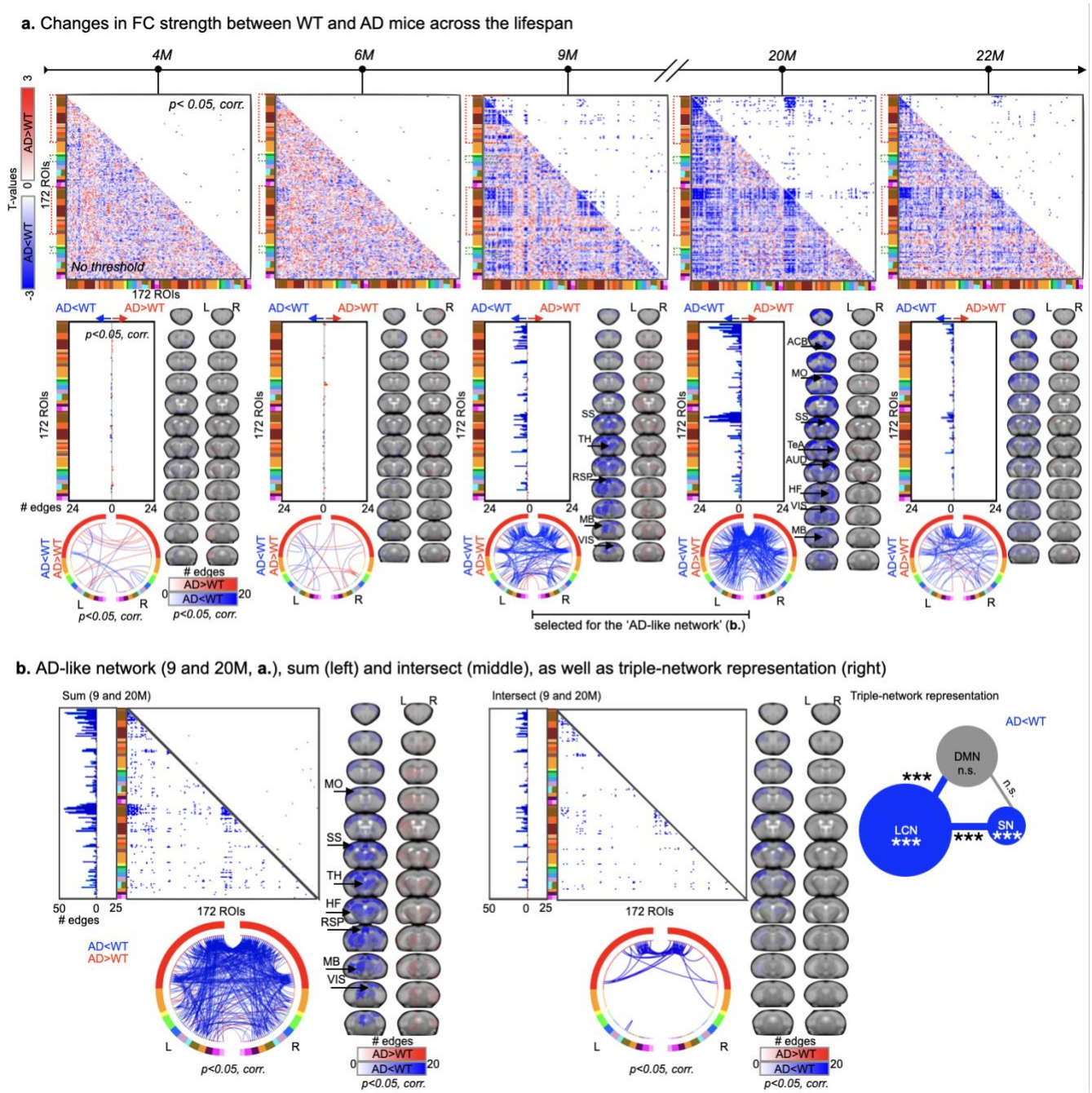

Fig. 4| Emerging at 9M, AD mice show a pronounced decrease in FC strength relative to WT mice. (**a.**) As in **Fig. 2** except here, we compare WT to AD groups at each timepoint. Positive t-values (red) indicate greater FC strength in AD vs. WT mice. Negative values (blue) indicate the opposite. (**b.**) As in **Fig. 3** except here, we collapse across 9 and 20M timepoints (as indicated in **a.**). Significance is displayed as * for p<0.05, ** for p<0.01 and *** for p<0.001.

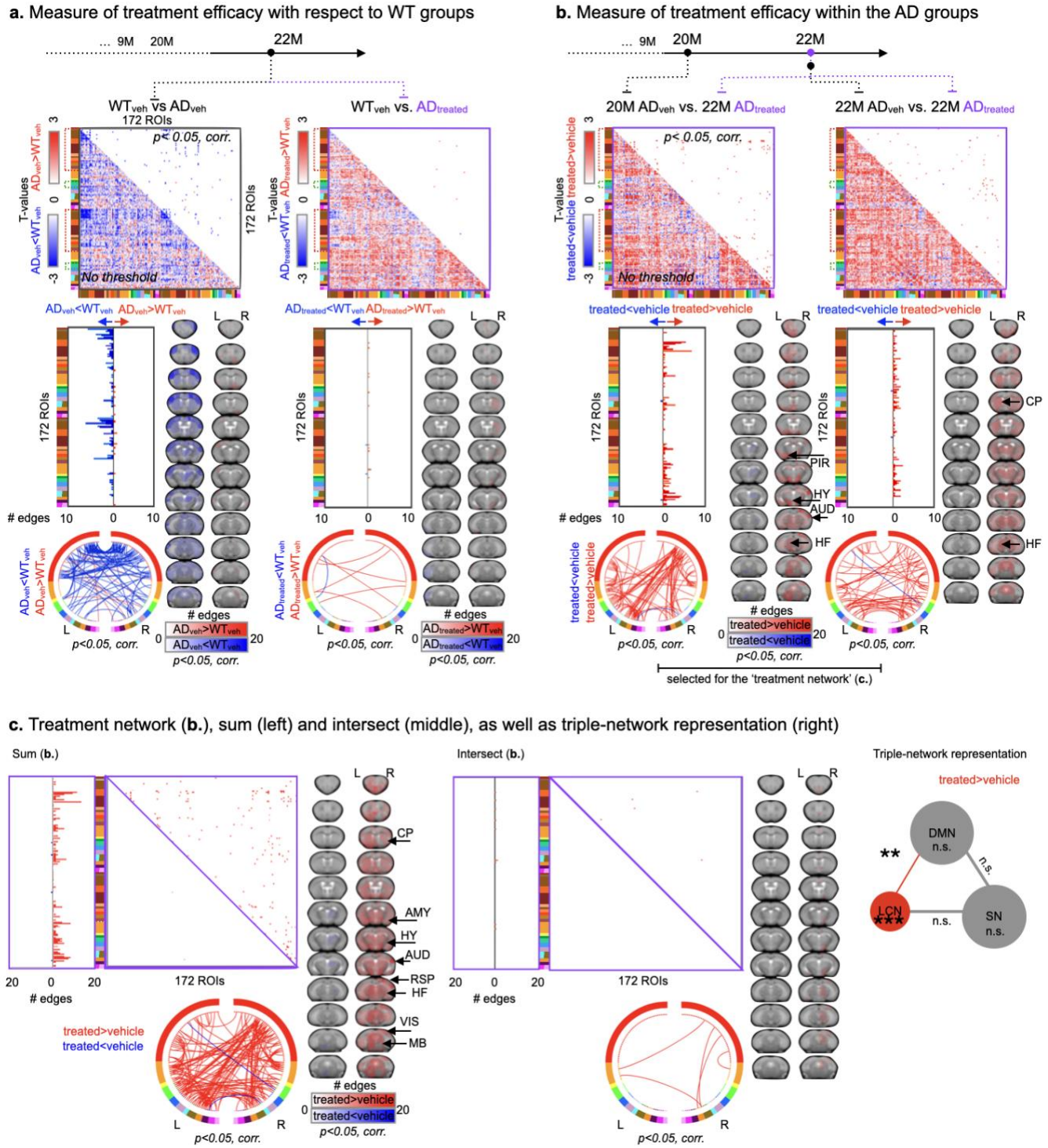

Fig. 5| BMS-984923 treatment rescues FC deficits in $AD_{treated}$ mice. (**a.**) Differences in FC strength between $WT_{vehicle}$ and $AD_{vehicle}$ (left, replicated from **Fig. 4a**) as well as $WT_{vehicle}$ and $AD_{treated}$ (right) at 22M. Positive t-values (red) indicate increased FC strength in $AD_{vehicle}$ vs. WT mice (left) or increased FC strength in $AD_{treated}$ vs. WT mice (right). Negative t-values (blue) indicated decreased FC strength in $AD_{vehicle}$ vs. mice (left) or decreased FC strength in $AD_{treated}$ vs. WT mice (right). BMS-984923 treatment appears to globally reduce FC strength differences between groups at 22M (two-sampled t-test, MATLAB, ttest2). (**b.**) Treatment effects in $AD_{treated}$ (22M) relative to age-matched $AD_{vehicle}$ mice (right) or $AD_{vehicle}$ mice at 20M (left). Positive t-values (red) indicate increased FC in $AD_{treated}$ vs. $AD_{vehicle}$ mice. Negative t-values (blue) indicate decreased FC strength in $AD_{treated}$ vs. $AD_{vehicle}$ mice. (**c.**) As in **Fig. 3** and **Fig. 4b** except here, we collapse across treatment effects (as indicated in **b.**). Significance is displayed as * for p<0.05, ** for p<0.01 and *** for p<0.001. VIS: visual cortex, AUD: auditory cortex, HF: hippocampal formation, HY: hypothalamus, AMY: amygdala, CP: caudoputamen.

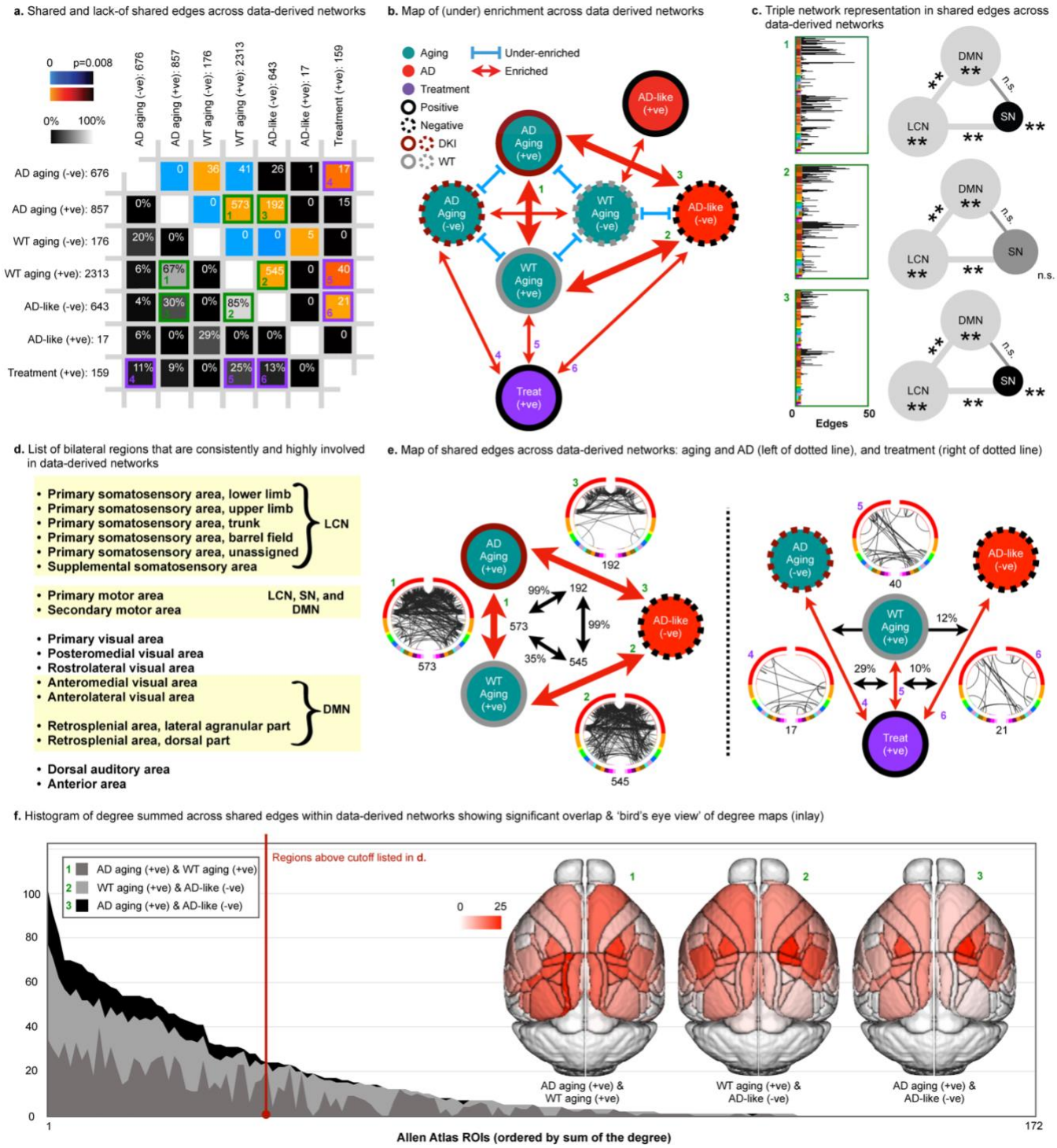

Fig. 6| Shared functional anatomy of data-derived networks. (**a.**) Greyscale lower left: the fraction of shared edges between data-derived networks computed as the fraction of the smaller network contained within the larger network (e.g., 85% of the 643 edges within the AD-like (-ve) network are within the 2,313 edges within the WT-aging (+ve) network). Color upper right: Using Fisher's exact test (corrected, permutation test x1,000), we determine if a significant number of shared edges (hot colors), or a significant ($p<0.008$) lack of shared edges (cool colors), are found between data-derived network pairs. White numbers in each cell are the number of shared edges. (**b.**) Schematic of overlap (red arrows) and lack of overlap (blue lines with caps) between data-derived networks. Arrow size is proportional to significance. (**c.**) Edges shared between AD-aging (+ve), WT-aging (+ve), and AD-like (-ve) pairs – green: 1, 2, and 3 – are shown as vertical ROI plots and ball-and-stick diagrams. (**e.**) Schematic of overlap between two groupings of edges that are shared across data-derived networks: Age and AD (left of dotted line, green: 1, 2, and 3), and treatment (right of dotted line, purple: 4, 5, and 6). No significant representation of edges shared across data-derived networks including the treatment network – purple: 4, 5, and 6 – is found with the triple-network system (DMN, LCN, or SN). Bilateral regions that are identified consistently (in 1, 2, and 3) which show the highest degree are listed (**d.**). A layered histogram of degree for the 1, 2, and 3 grouping (**f.**) with a bird's eye view of a degree color-map (red), in-lay. Significance is displayed as * for $p<0.05$, ** for $p<0.01$ and *** for $p<0.001$.

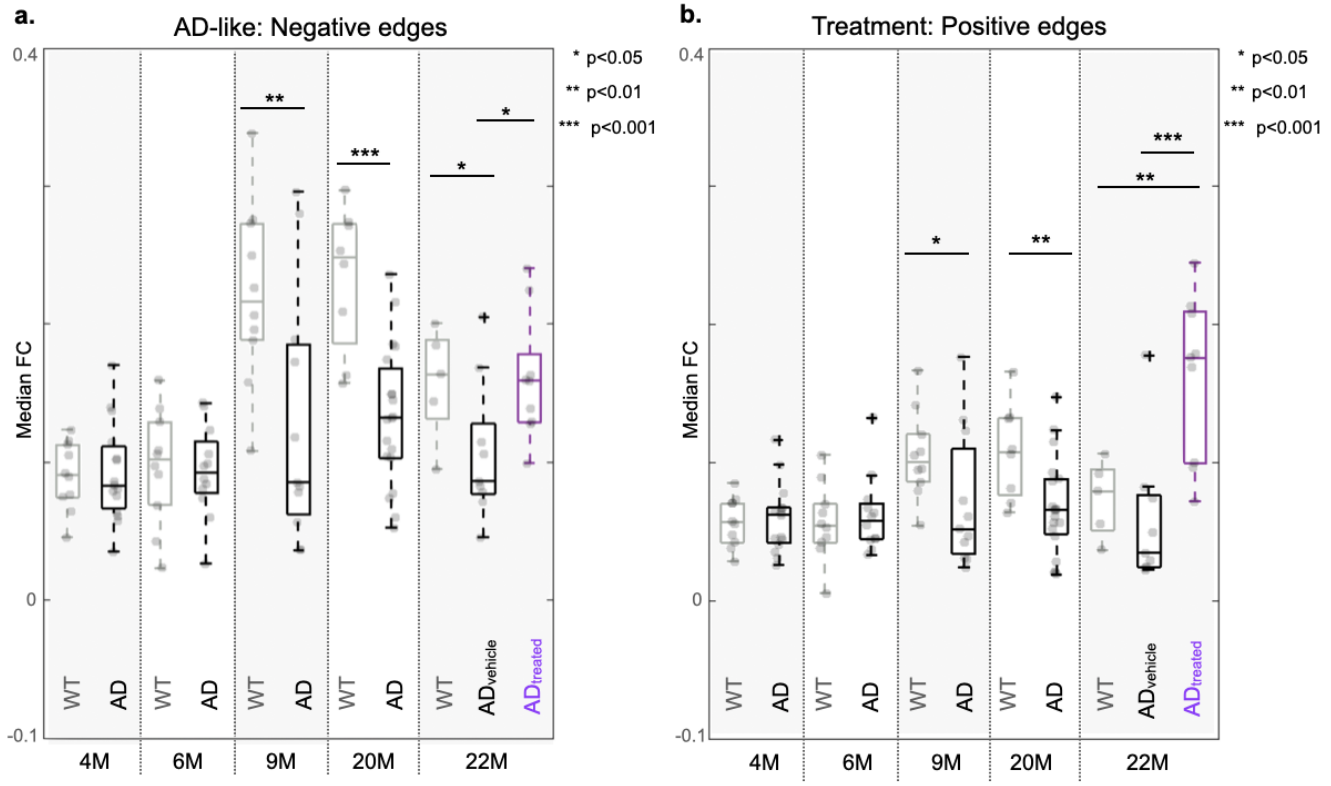

Fig. 7| Mean FC within data-derived networks. Median FC computed by multiplying data-derived networks by connectomes obtained from each mouse at each imaging timepoint. Boxplots are shown for WT (grey), and AD (vehicle/treated black/red) mice, for AD-like (-ve) (**a.**) and treatment (+ve) (**b.**) networks. A t-test is used to compare median FC strengths across groups, at each timepoint. For the 22M timepoint, an ANOVA is performed first, and t-tests are computed after to check the level of the significance found. Significance is displayed as * for p<0.05, ** for p<0.01, and *** for p<0.001.

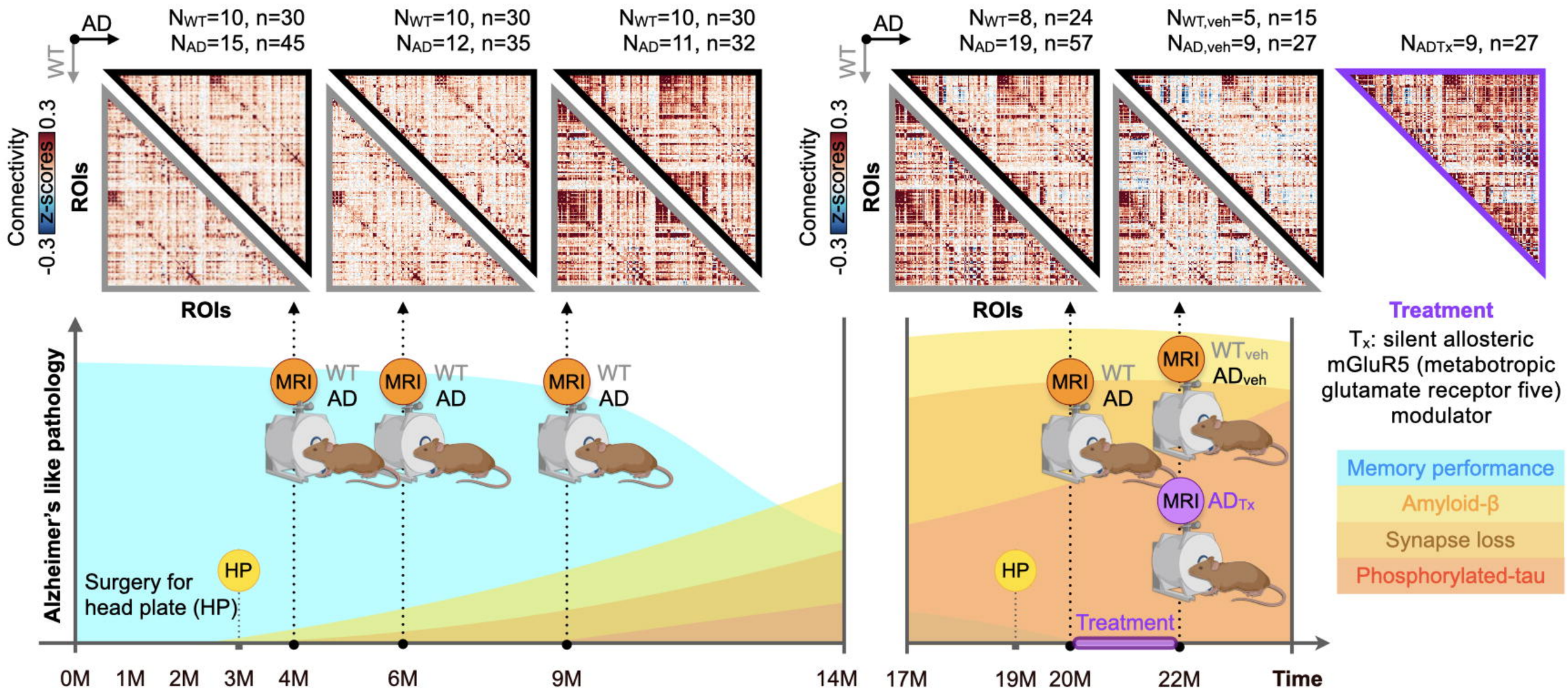
AD
WT
N_{WT}=10, n=30
N_{AD}=15, n=45
N_{WT}=10, n=30
N_{AD}=12, n=35
N_{WT}=10, n=30
N_{AD}=11, n=32
N_{WT}=8, n=24
N_{AD}=19, n=57
$N_{WT,veh}$=5, n=15
$N_{AD,veh}$=9, n=27
N_{ADTx}=9, n=27
Connectivity
Z-scores
0.3
-0.3
ROIs
Alzheimer's like pathology
MRI
WT
AD
WT_{veh}
AD_{veh}
AD_{Tx}
HP
Surgery for head plate (HP)
Treatment
0M
1M
2M
3M
4M
6M
9M
14M
17M
19M
20M
22M
Time
Treatment
T_x: silent allosteric mGluR5 (metabotropic glutamate receptor five) modulator
Memory performance
Amyloid-β
Synapse loss
Phosphorylated-tau

a. Changes in FC strength with age in WT mice across the lifespan

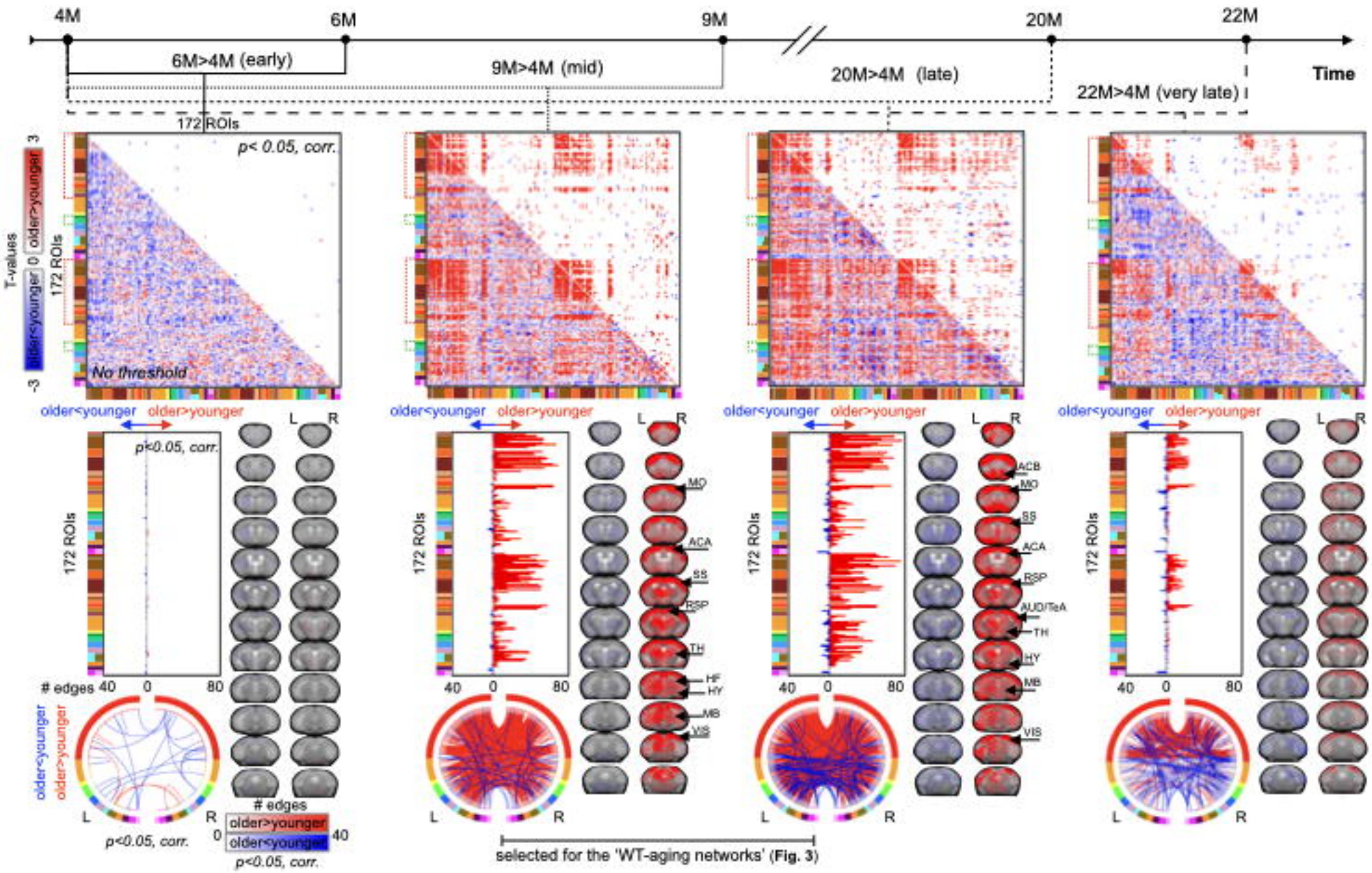

b. Changes in FC strength with age in AD mice across the lifespan

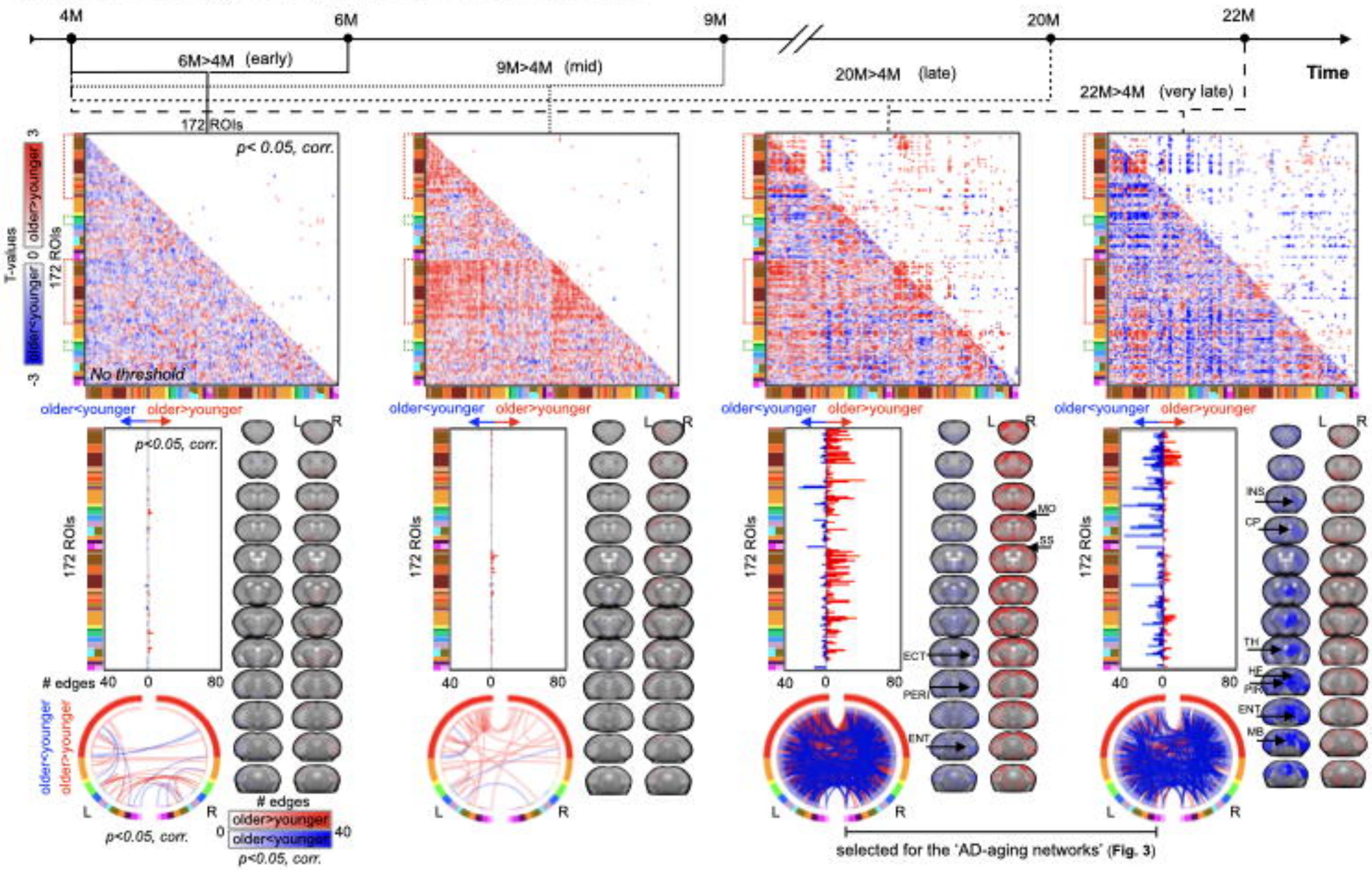

a. WT-aging networks (mid- & late- stages, **Fig. 2**), sum (left) and intersect (middle), as well as triple-network representation (right)

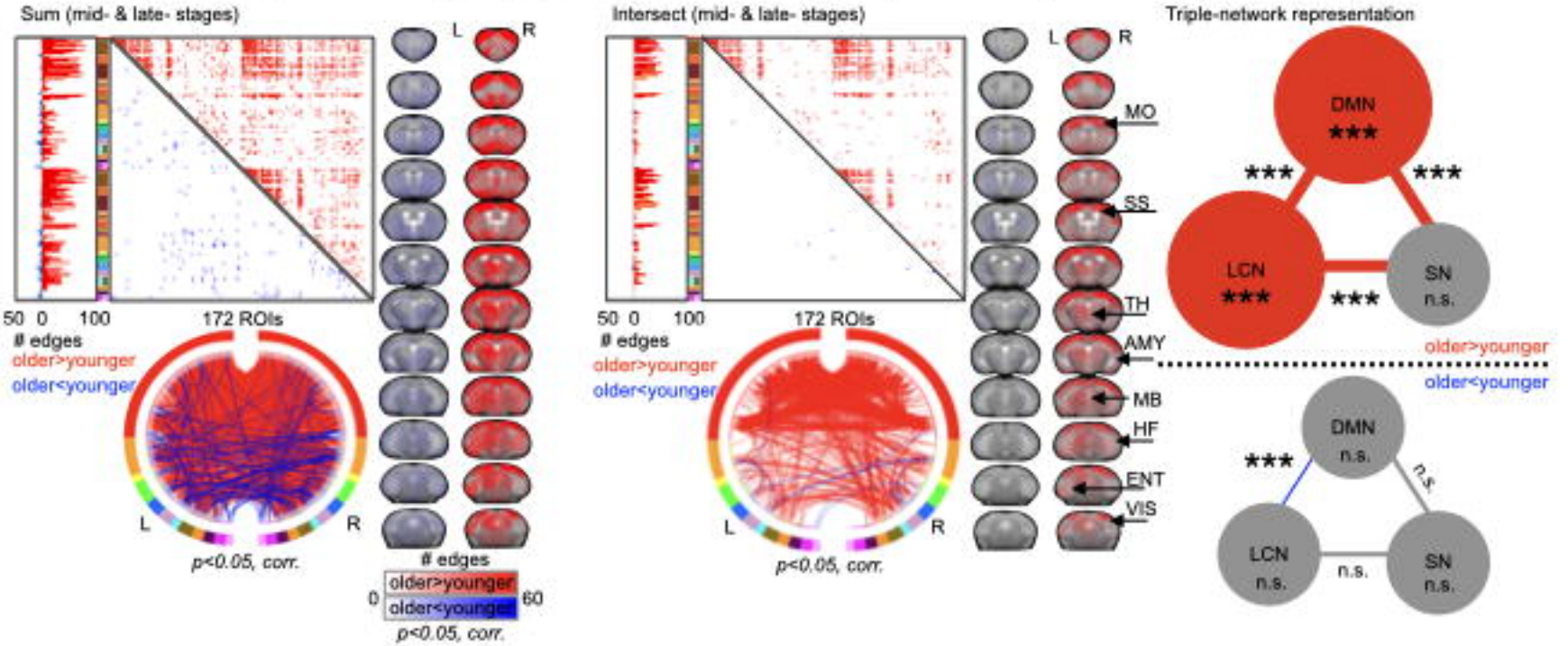

b. AD-aging networks (late- & very late- stages, **Fig. 2**), sum (left) and intersect (middle), as well as triple-network representation (right)

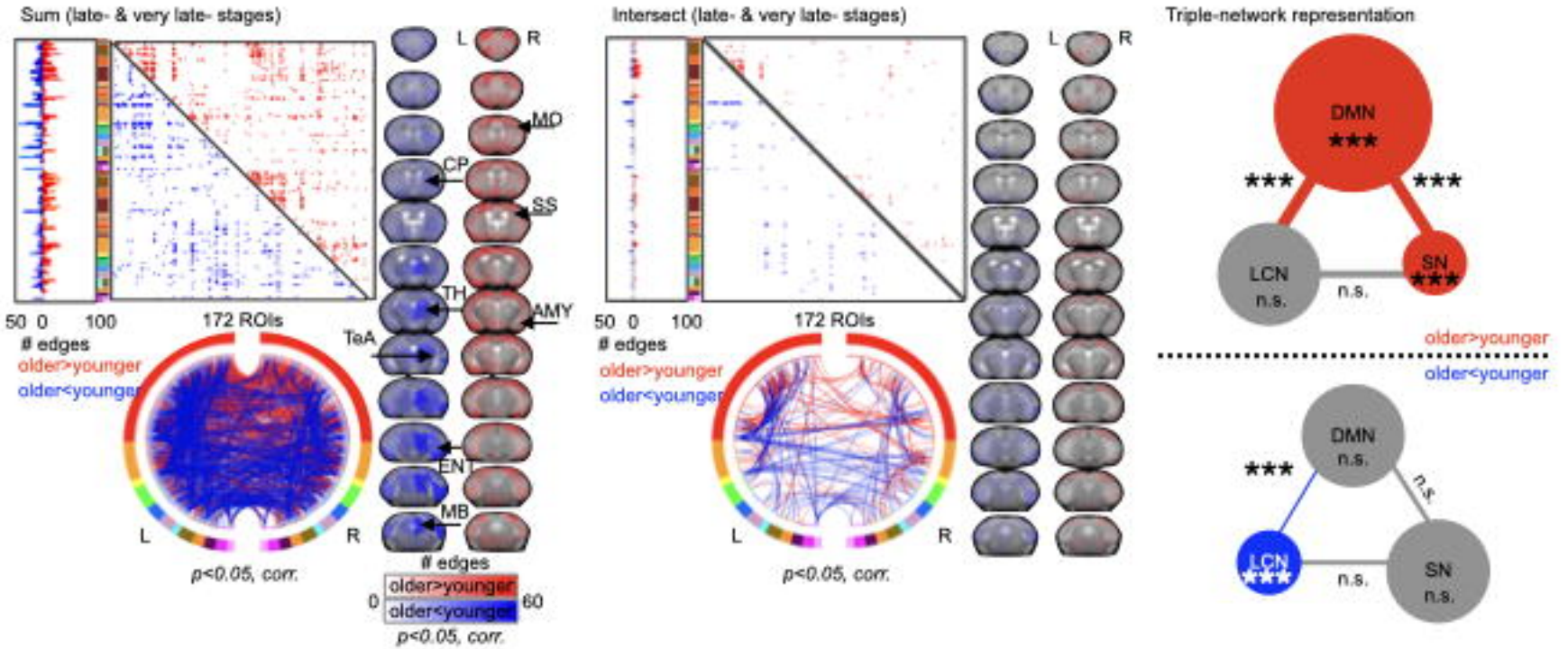

a. Changes in FC strength between WT and AD mice across the lifespan

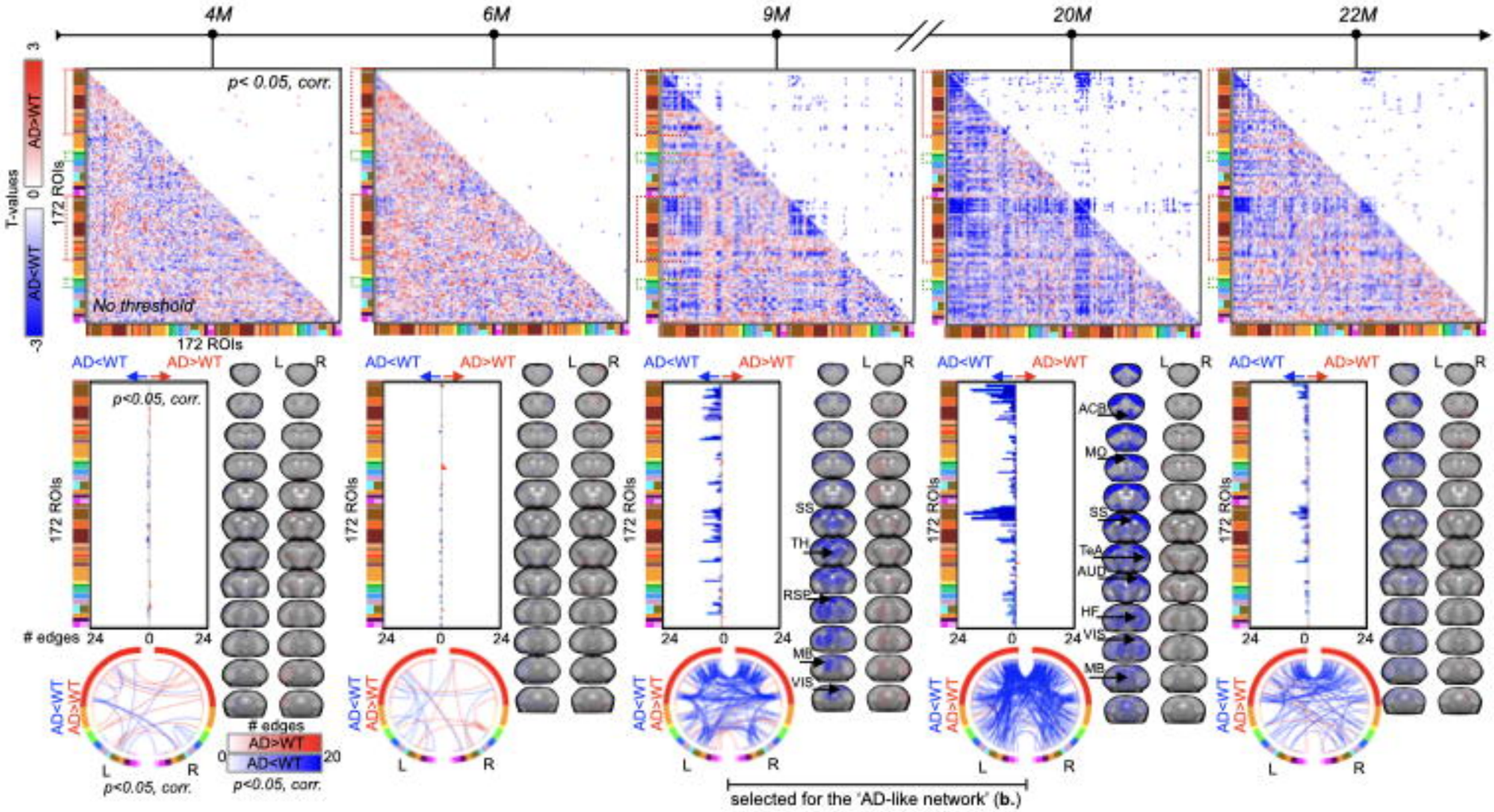

b. AD-like network (9 and 20M, **a.**), sum (left) and intersect (middle), as well as triple-network representation (right)

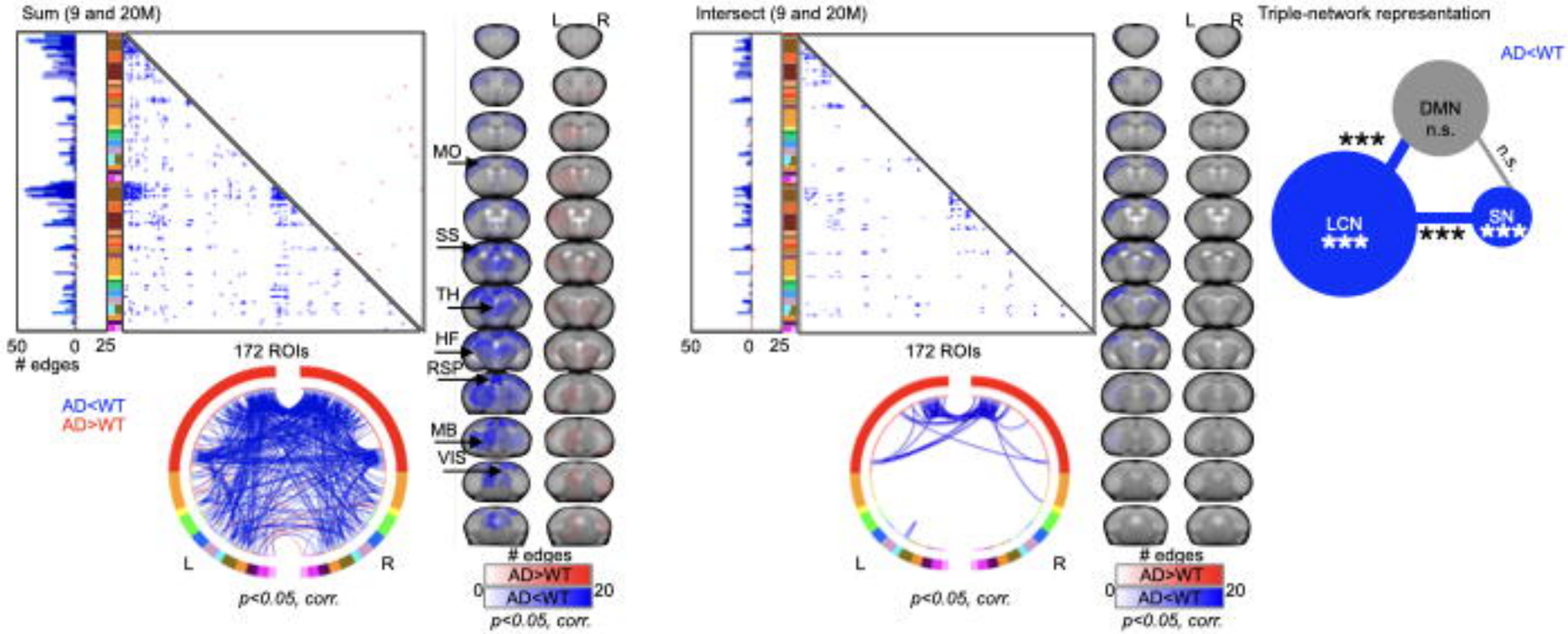

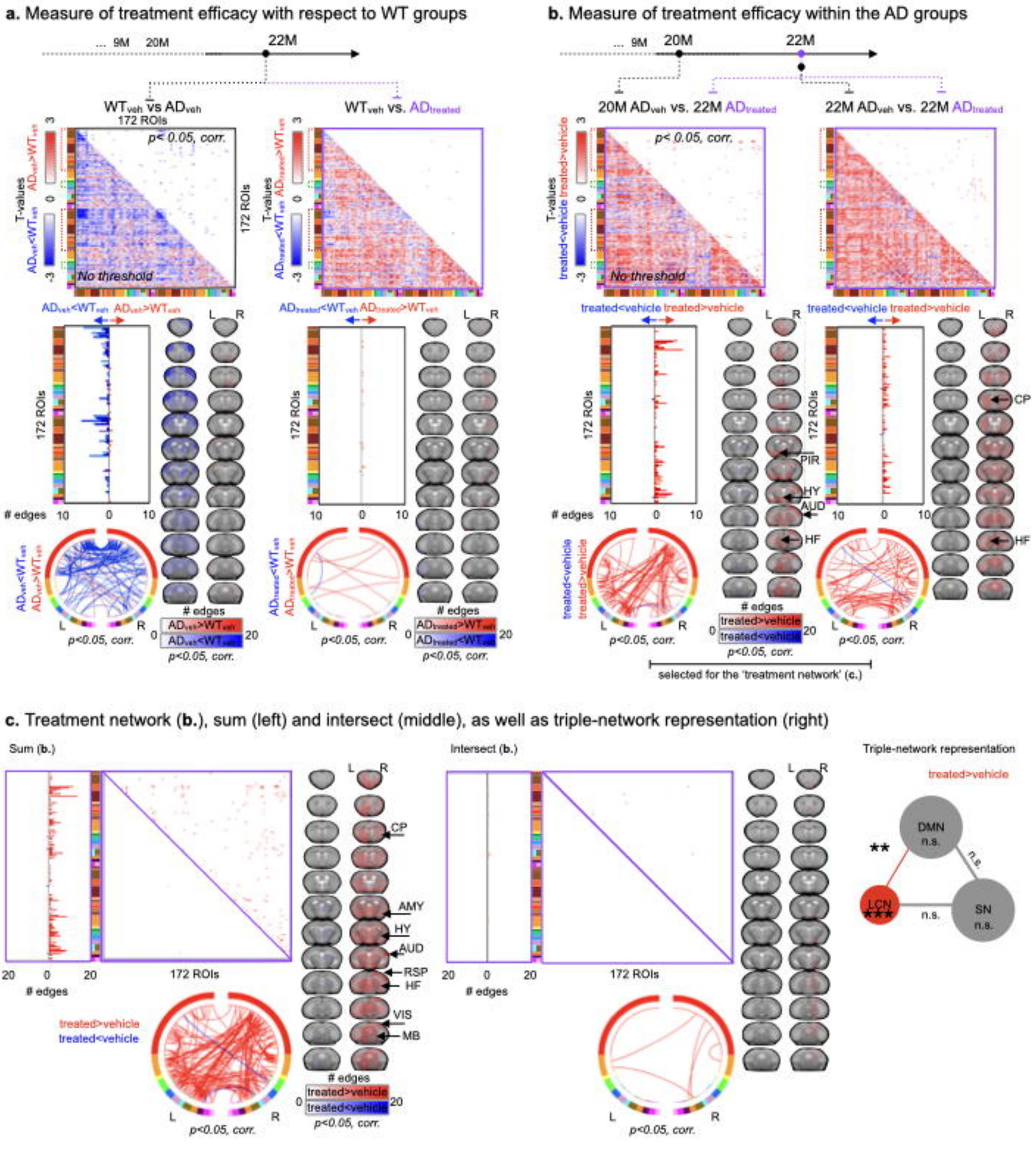
a. Measure of treatment efficacy with respect to WT groups
b. Measure of treatment efficacy within the AD groups
... 9M 20M 22M
WTveh vs ADveh
WTveh vs. ADtreated
20M ADveh vs. 22M ADtreated
22M ADveh vs. 22M ADtreated
172 ROIs
p< 0.05, corr.
No threshold
T-values
ADveh<WTveh ADveh>WTveh
ADtreated<WTveh ADtreated>WTveh
treated<vehicle treated>vehicle
edges
L R
CP
PIR
HY
AUD
HF
p<0.05, corr.
selected for the 'treatment network' (c.)
c. Treatment network (b.), sum (left) and intersect (middle), as well as triple-network representation (right)
Sum (b.)
Intersect (b.)
Triple-network representation
treated>vehicle
DMN n.s.
LCN ***
SN n.s.
n.s.
**
AMY
RSP
VIS
MB

a. Shared and lack-of shared edges across data-derived networks

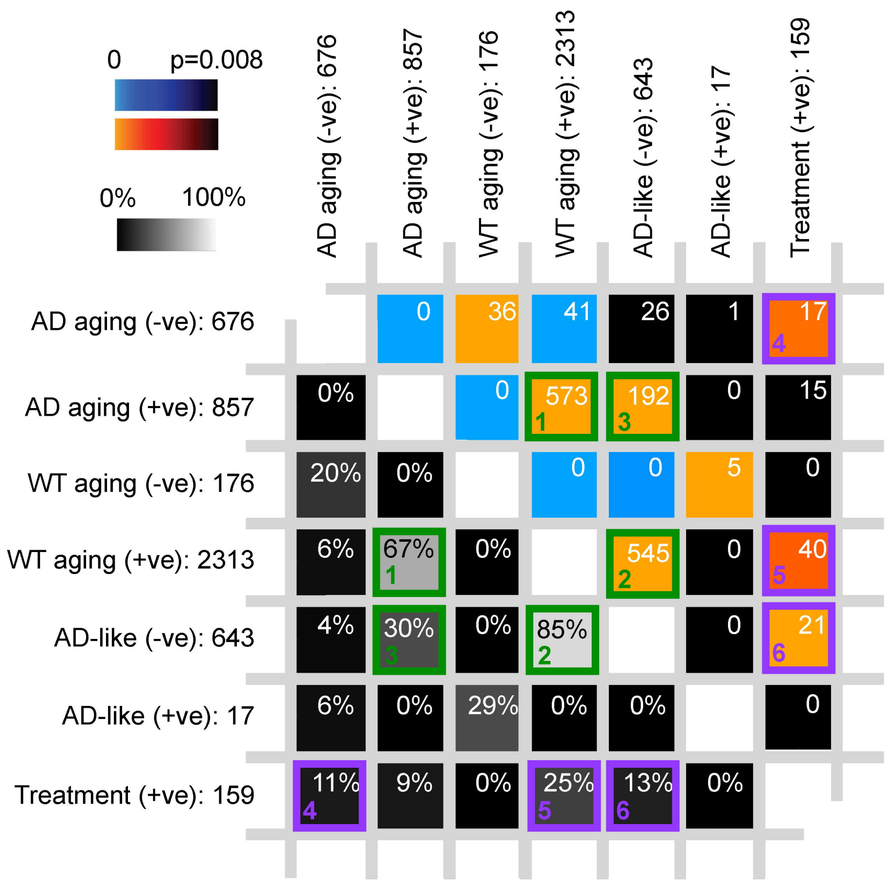

b. Map of (under) enrichment across data derived networks

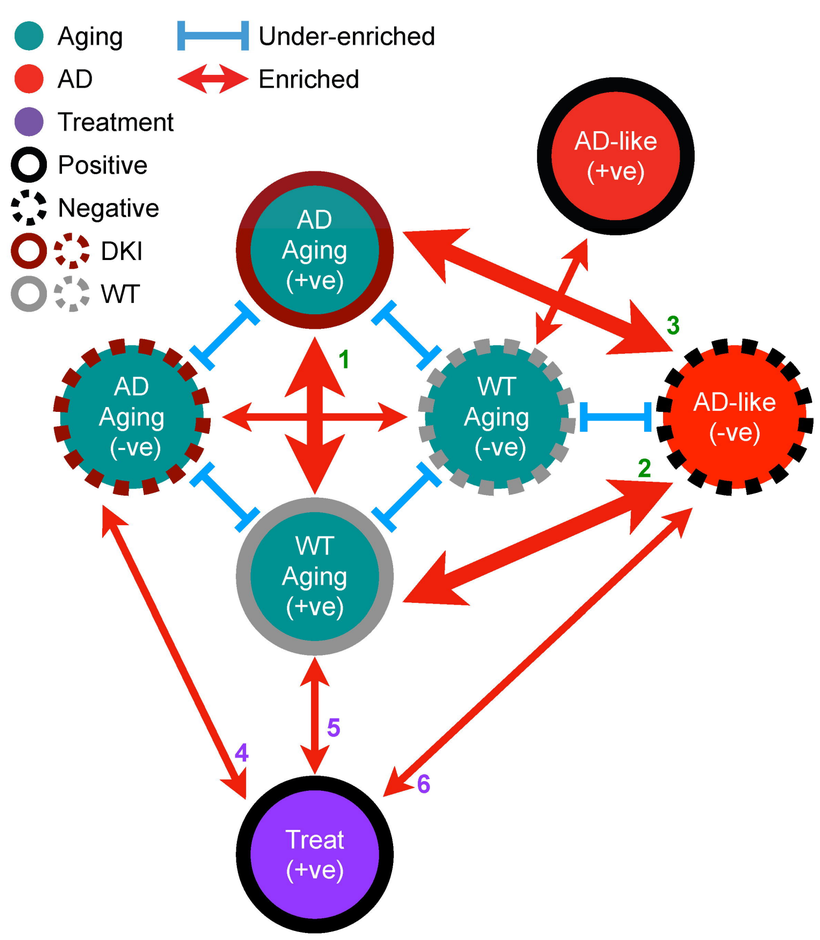

c. Triple network representation in shared edges across data-derived networks

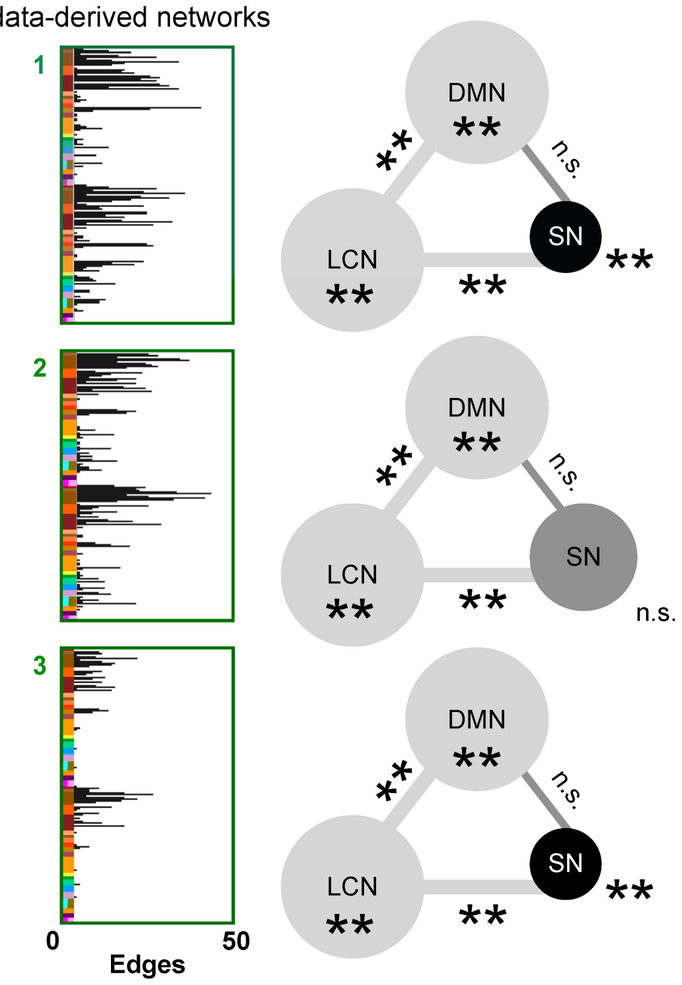

d. List of bilateral regions that are consistently and highly involved in data-derived networks

- **Primary somatosensory area, lower limb**
- **Primary somatosensory area, upper limb**
- **Primary somatosensory area, trunk**
- **Primary somatosensory area, barrel field**
- **Primary somatosensory area, unassigned**
- **Supplemental somatosensory area**

} **LCN**

- **Primary motor area**
- **Secondary motor area**

LCN, SN, and DMN

- **Primary visual area**
- **Posteromedial visual area**
- **Rostrolateral visual area**
- **Anteromedial visual area**
- **Anterolateral visual area**
- **Retrosplenial area, lateral agranular part**
- **Retrosplenial area, dorsal part**

} **DMN**

- **Dorsal auditory area**
- **Anterior area**

e. Map of shared edges across data-derived networks: aging and AD (left of dotted line), and treatment (right of dotted line)

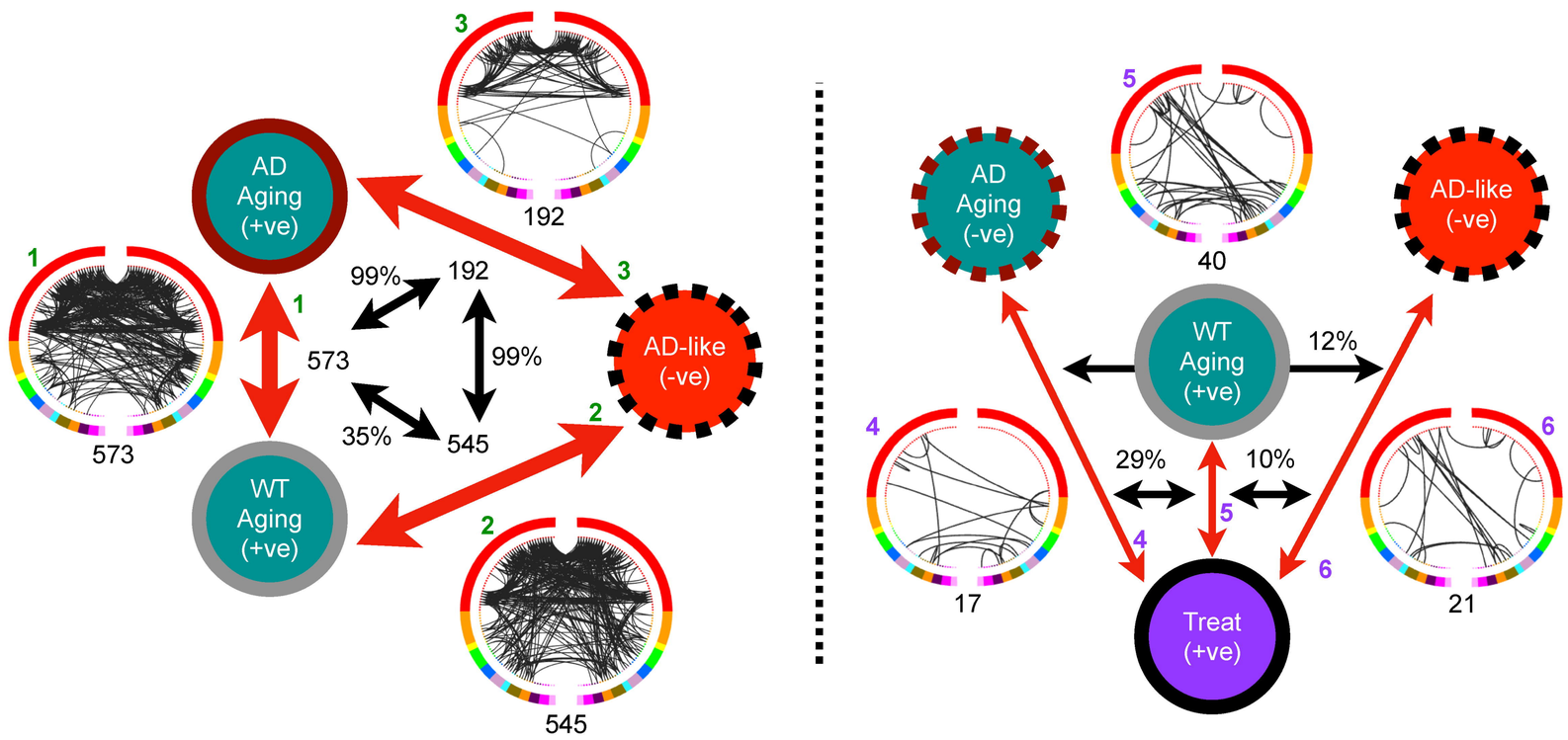

f. Histogram of degree summed across shared edges within data-derived networks showing significant overlap & 'bird's eye view' of degree maps (inlay)

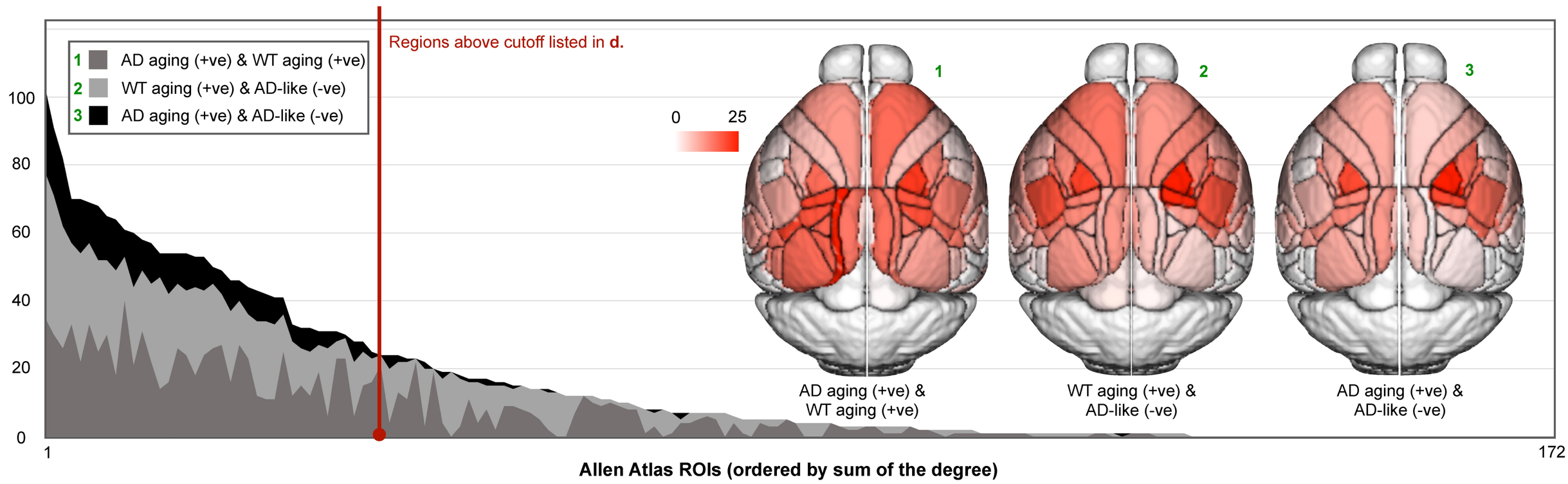

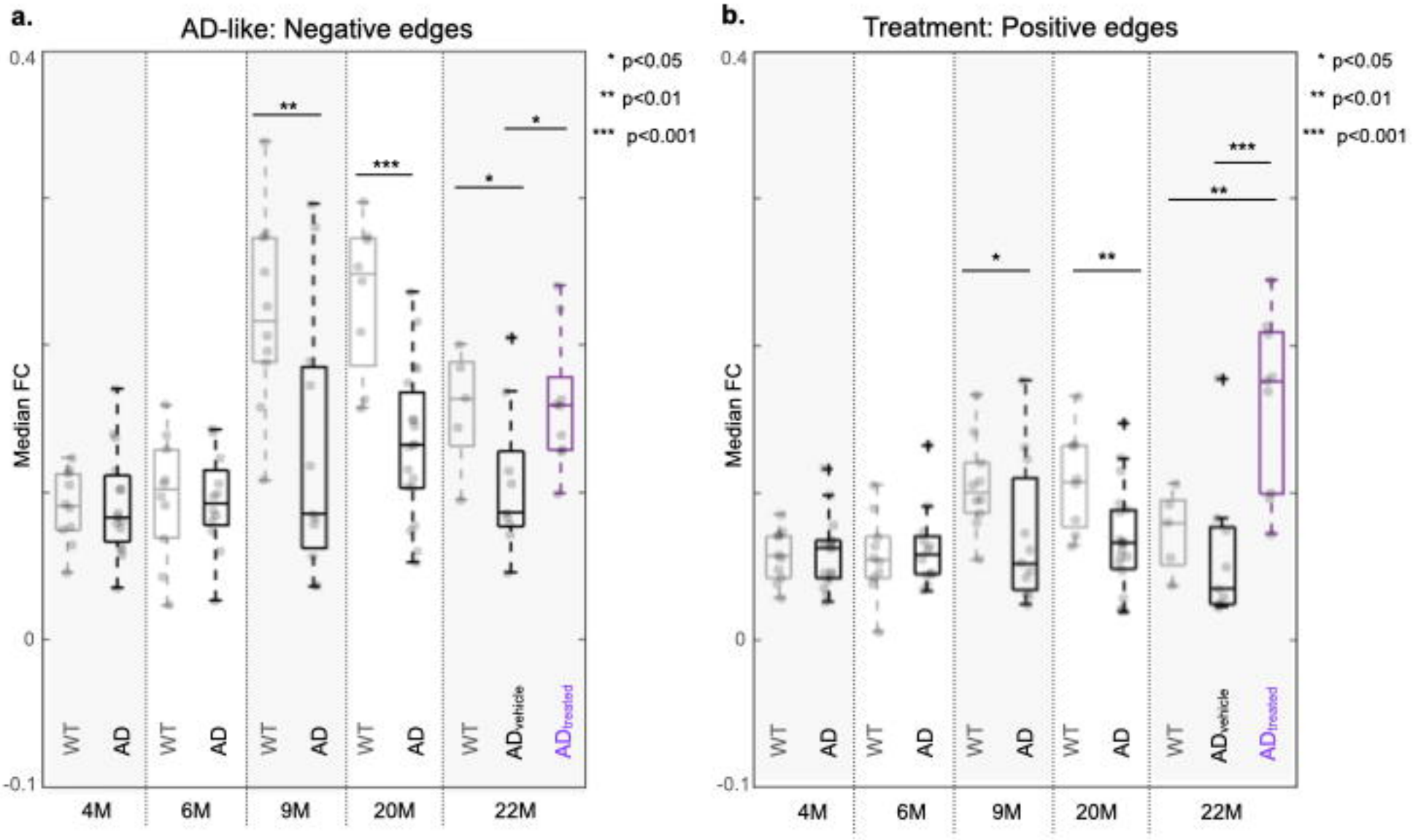
a.
AD-like: Negative edges
b.
Treatment: Positive edges
* p<0.05
** p<0.01
*** p<0.001
Median FC
0.4
0
-0.1
WT
AD
ADvehicle
ADtreated
4M
6M
9M
20M
22M